

# Temporal transitions in the post-mitotic nervous system of *Caenorhabditis elegans*

<https://doi.org/10.1038/s41586-021-04071-4>

HaoSheng Sun<sup>1,2✉</sup> & Oliver Hobert<sup>1✉</sup>

Received: 9 October 2020

Accepted: 29 September 2021

Published online: 10 November 2021

 Check for updates

In most animals, the majority of the nervous system is generated and assembled into neuronal circuits during embryonic development<sup>1</sup>. However, during juvenile stages, nervous systems still undergo extensive anatomical and functional changes to eventually form a fully mature nervous system by the adult stage<sup>2,3</sup>. The molecular changes in post-mitotic neurons across post-embryonic development and the genetic programs that control these temporal transitions are not well understood<sup>4,5</sup>. Here, using the model system *Caenorhabditis elegans*, we comprehensively characterized the distinct functional states (locomotor behaviour) and the corresponding distinct molecular states (transcriptome) of the post-mitotic nervous system across temporal transitions during post-embryonic development. We observed pervasive, neuron-type-specific changes in gene expression, many of which are controlled by the developmental upregulation of the conserved heterochronic microRNA LIN-4 and the subsequent promotion of a mature neuronal transcriptional program through the repression of its target, the transcription factor *lin-14*. The functional relevance of these molecular transitions are exemplified by a temporally regulated target gene of the LIN-4 transcription factor, *nlp-45*, a neuropeptide-encoding gene, which we find is required for several distinct temporal transitions in exploratory activity during post-embryonic development. Our study provides insights into regulatory strategies that control neuron-type-specific gene batteries to modulate distinct behavioural states across temporal, sexual and environmental dimensions of post-embryonic development.

In most non-metamorphosing invertebrates and vertebrates, including mammals, the majority of neurons of the adult nervous system are born and differentiate during embryogenesis, forming a functional, yet immature nervous system by the time of birth/hatch<sup>1</sup>. During post-embryonic stages of life, juvenile nervous systems undergo substantial maturation events that have mostly been characterized at the anatomical and electrophysiological level<sup>2,3</sup>. However, there have been few systematic efforts to characterize the molecular changes within post-mitotic neurons during post-embryonic development<sup>4,5</sup>. It also remains unclear whether post-embryonic, post-mitotic maturation of neurons is mostly a reflection of neuronal activity changes<sup>6,7</sup> or whether there are activity-independent genetic programs that mediate these temporal transitions. Earlier-acting genetic programs that control the specification of the temporal identity of dividing neuroblasts have been characterized in both vertebrates and *Drosophila*<sup>8–11</sup>. However, the genetic programs that may specify temporal transitions in post-mitotic neurons during post-embryonic development have remained unclear.

At hatching, the juvenile nervous system of the nematode *C. elegans* contains the vast majority of its adult set of neurons (97 out of 118 hermaphrodite neuron classes), most of which are fully differentiated and wired into a functional nervous system<sup>12</sup>. To systematically characterize potential changes in nervous system function during post-embryonic

neuronal development, we profiled locomotor behaviour across all four larval stages as well as the adult stage of the hermaphrodite using an automated, high-resolution worm-tracking system<sup>13</sup>. We observed pervasive changes across all four larval stages into adulthood (Fig. 1a and Supplementary Table 1). For example, animals at the second larval (L2) stage exhibited increased pausing and dwelling behaviour compared to animals at the first larval (L1) stage, whereas adult animals exhibited increased forward motion and decreased backward motion compared with animals at the last larval stage (L4).

Distinct behavioural states across post-embryonic life stages, as well as the recently described synaptic wiring changes across post-embryonic development<sup>12</sup>, suggest the existence temporal transitions in molecular states. We profiled the transcriptome of the entire nervous system using isolation of nuclei from tagged specific cell types (INTACT) technology<sup>14,15</sup> during all post-embryonic stages, and we identified 7,974 neuronally enriched genes with temporal changes (Extended Data Fig. 1a and Supplementary Tables 2 and 3). Principal-component analysis revealed that the neuronal transcriptome of each developmental stage clustered together and was distinct from the other stages (Fig. 1b, c, Extended Data Fig. 1b–d and Supplementary Discussion). Gene Ontology analysis of the developmentally regulated genes revealed an expected enrichment in nervous-system-associated

<sup>1</sup>Department of Biological Sciences, Howard Hughes Medical Institute, Columbia University, New York, NY, USA. <sup>2</sup>Present address: Department of Cell, Developmental and Integrative Biology, Heersink School of Medicine, University of Alabama at Birmingham, Birmingham, AL, USA. ✉e-mail: sunh@uab.edu; or38@columbia.edu

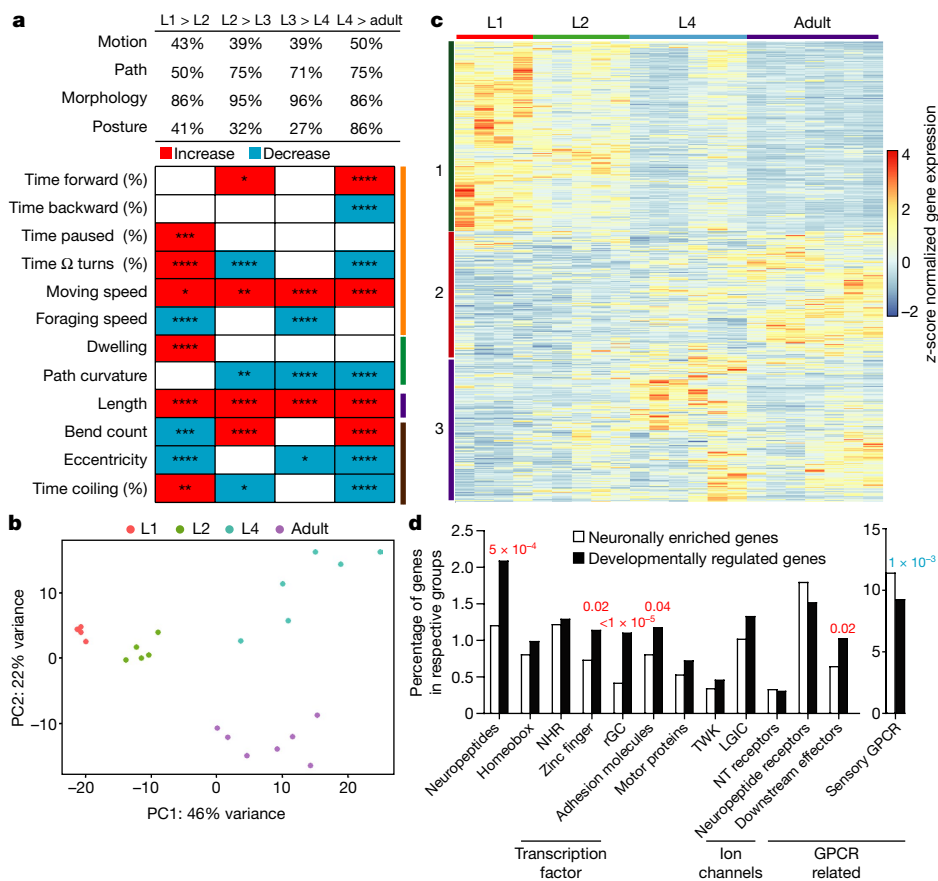


**Fig. 1 | Temporal transitions in locomotor behaviour and the neuronal transcriptome.** **a**, Developmental transition in locomotor behaviour across post-embryonic life stages, as measured by automated single-worm tracking<sup>13</sup>. Top, the percentage of parameters in each of the four broad categories that are different across each transition ( $q < 0.05$ ). Bottom, representative parameters from each category, as indicated by colour-coded lines on the right, across development. The red and blue rectangles indicate increases and decreases in each parameter, respectively.  $n = 47$  (L1);  $n = 48$  (L2);  $n = 41$  (L3);  $n = 129$  (L4);  $n = 107$  (adult). Statistical analysis was performed using Wilcoxon rank-sum tests, and false-discovery-rate-adjusted  $q$  values for each comparison are presented in each rectangle; \* $q < 0.05$ ; \*\* $q < 0.01$ ; \*\*\* $q < 0.001$ ; \*\*\*\* $q < 0.0001$ . Additional details are provided in Supplementary Table 1. **b**, Principal component analysis (DESeq2) of the neuronal transcriptome across

genes (Extended Data Fig. 1e–j and Supplementary Tables 4 and 5). Specific gene families were over-represented among the developmentally regulated genes, including neuropeptides, receptor-type guanylyl cyclases (rGC), zinc-finger transcription factors and cell-adhesion molecules, that may drive the recently reported changes in synaptic wiring occurring during post-embryonic development<sup>12</sup> (Fig. 1d).

Owing to the pan-neuronal nature of our profiling, increases or decreases in gene expression could entail binary on/off switches in individual neuron types and/or relative changes in the levels of expression in the same set of neurons. Using gene expression reporters that detect changes at the single-neuron resolution (many of them endogenous reporter alleles engineered with CRISPR–Cas9 technology), we found ample evidence for both scenarios and near-perfect validation of our RNA-sequencing dataset (Extended Data Figs. 2–4 and Supplementary Table 6). For example, the expression of the glutamate receptor *gbb-2* decreased in all expressing cells throughout larval development (Extended Data Fig. 2a), whereas expression of the innexin *inx-19* was progressively lost from specific neuron types throughout larval stages (Extended Data Fig. 2b). Moreover, we detected uniform changes in the expression of broadly expressed

post-embryonic development. Each dot represents a RNA-seq analysis replicate. **c**, Heat map of the 2,639 developmentally regulated genes ( $P_{adj} < 0.01$ ) across post-embryonic life stages. Values were z-score normalized and plotted using pheatmap in R studio. Each row, clustered according to pattern, represents a single gene, and each column represents a single RNA-seq replicate. **d**, Enrichment or depletion of gene families in the 2,639 developmentally regulated genes compared to all 7,974 neuronal enriched genes (one-sided z-score test for two-population proportions); the red and blue  $P$  values indicate overrepresentation and underrepresentation, respectively. GPCR, G-protein-coupled receptor; LGIC, ligand-gated ion channel; NHR, nuclear hormone receptor; NT, neurotransmitter; TWK, two-pore domain potassium.

genes (such as *mab-10*) (Extended Data Fig. 2c). We also found changes in the expression of highly restrictively expressed genes that were up- or downregulated in a small subset of neurons or even in a single neuron class (such as *ins-6*) (Extended Data Fig. 3c). Additional validations of neuron-type-specific changes that recapitulate all major patterns of developmental regulation are documented in Extended Data Figs. 2–4 and Supplementary Table 6. Changes were observed in neurons of all major types.

To investigate the regulation of these temporal transitions, we considered the heterochronic pathway—a cascade of microRNAs (miRNAs), RNA-binding proteins and transcription factors that were initially discovered to regulate temporal developmental progression in mitotic ectodermal lineages and the reproductive system<sup>16–19</sup>. Upregulation of the conserved microRNA *lin-4* at the L1-to-L2 transition promotes later-stage cellular identities and suppresses early (L1/juvenile) identities through 3′-UTR-mediated downregulation of its direct target, the transcription factor *lin-14* (refs. 18,19; Fig. 2a). Using a fosmid-based reporter gene and/or CRISPR–Cas9-engineered reporter alleles, we validated the expression dynamics of *lin-4* and *lin-14* in the context of the nervous system (Extended Data Fig. 5).

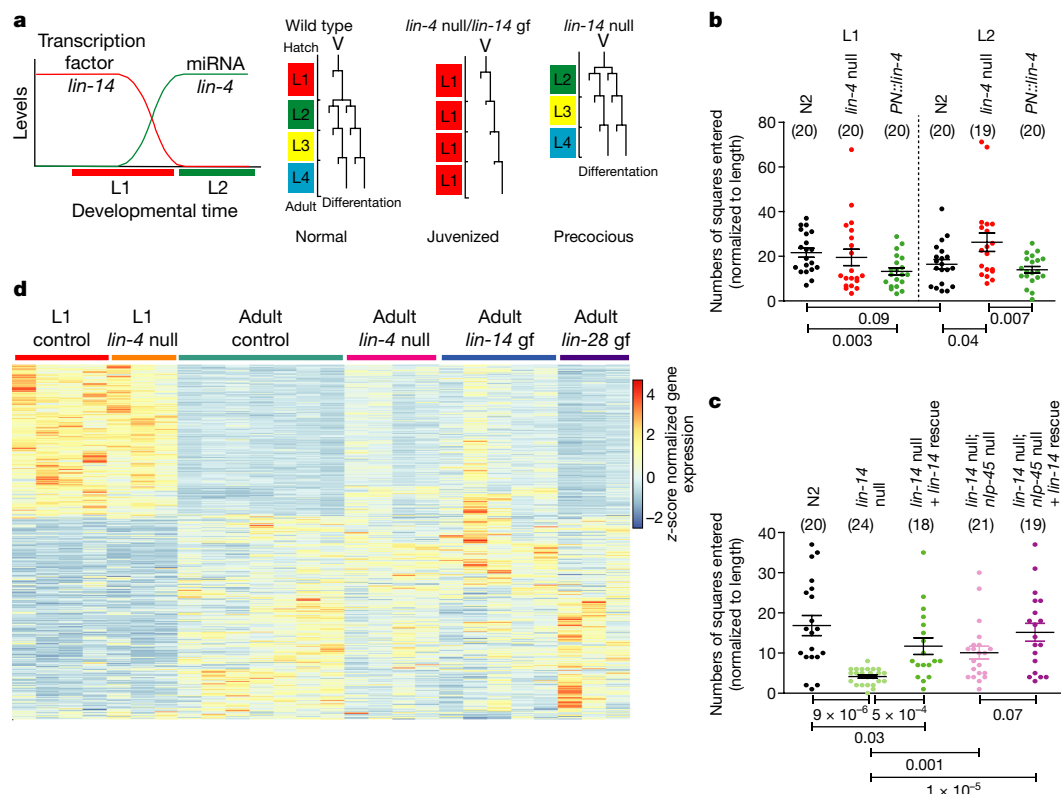


**Fig. 2** | *lin-4* and *lin-14* control temporal transitions in exploratory behaviour and neuronal transcriptome. **a**, Schematic of *lin-4* and *lin-14* expression and function in the context of epithelial/hypodermal lineages, revealing reiterated juvenized lineage patterns in *lin-4*-null and *lin-14*-gain-of-function (gf) mutants and precocious patterns in *lin-14*-null mutants. **b**, Neuronal *lin-4* regulates the ‘maturation’ of exploratory behaviour during the L1-to-L2 transition. Exploratory behaviour was measured as shown in Extended Data Fig. 10a. PN::*lin-4* represents pan-neuronal *lin-4* overexpression. **c**, *lin-14*(*mal135*)-null mutants exhibit precocious exploratory behaviour through the

regulation of *nlp-45*. Exploratory behaviour was measured as described in Extended Data Fig. 10a. For **b** and **c**, data are mean  $\pm$  s.e.m. Each point represents a single animal. *n* values are shown in parentheses for each condition. Statistical analysis was performed using two-sided *t*-tests with post hoc corrections; *P* values are shown below. **d**, *lin-4*(*e912*)-null mutation juvenizes a subset of the adult control neuronal transcriptome to resemble that of the L1 control neuronal transcriptome through the direct derepression of *lin-14* (Extended Data Figs. 5b, 6a–e and 9 and Supplementary Discussion). The values displayed are as described in Fig. 1c.

Consistent with the notion that *lin-14* promotes a juvenile state of neuronal function that is suppressed by *lin-4* at later stages, we found that behavioural transitions in exploratory activity were partially juvenized (decreased dwelling and increased exploration) in *lin-4* mutants and that forced neuronal expression of *lin-4* at the L1 stage caused a precocious decrease in exploratory behaviour (Fig. 2b). Moreover, *lin-14*(*mal135*)-null animals reduced their exploratory behaviour, and this effect was rescued by resupplying *lin-14* (Fig. 2c).

To assess the effect of *lin-4* and *lin-14* on molecular transitions in the neuronal transcriptome, we again used INTACT and observed a juvenization of a subset of the neuronal transcriptome in adult *lin-4* mutant adults (Fig. 2d, Extended Data Fig. 6a–d, Supplementary Table 7 and Supplementary Discussion). An engineered *lin-4* gain-of-function allele that is unresponsive to *lin-4* (Extended Data Fig. 5b) largely recapitulated the juvenizing effect of the *lin-4*-null mutation (Fig. 2d and Extended Data Fig. 6a–d), demonstrating that *lin-4* acts through *lin-14* to affect the neuronal transcriptome. The lack of developmental regulation of other subsets of genes in response to *lin-4* and *lin-14* mutations (Extended Data Fig. 7) suggested that there must be additional mechanisms beyond the *lin-4*- and *lin-14*-triggered heterochronic pathway that regulate the temporal transition of the nervous system across development.

To further investigate the role of *lin-14* in the maturation of the neuronal transcriptome, we identified genomic sites of direct LIN-14 binding in L1 and L2 animals using chromatin immunoprecipitation followed by sequencing (ChIP-seq) (Extended Data Fig. 8a, Supplementary

Tables 8 and 9 and Supplementary Discussion). Motif analysis identified YGGAR as a consensus binding sequence for LIN-14 (Extended Data Fig. 8b). Amalgamating different methods of differential-binding analysis resulted in 3,466 neuronally enriched genes that showed decreased LIN-14 binding within 3 kb of the transcription start site across the L1-to-L2 transition (Extended Data Fig. 8c and Supplementary Tables 10 and 11). This overlapped with 60% of *lin-4*/*lin-14*-controlled developmentally upregulated genes (where LIN-14 acts as a repressor) and 49% of *lin-4*/*lin-14*-controlled developmentally downregulated genes (where LIN-14 acts as an activator) (Extended Data Fig. 8c–e).

To examine the effect of *lin-4* and *lin-14* on neuron-specific gene expression patterns at single-neuron resolution, we examined four neuropeptide-encoding genes (using CRISPR–Cas9-engineered reporter alleles) and one rGC-encoding gene, the developmental regulation of which were predicted by our transcriptome and ChIP-seq data to be controlled by *lin-4* and *lin-14* (Fig. 3a, Extended Data Fig. 9 and Supplementary Table 12). Our focus on neuropeptides was motivated by the overrepresentation of neuropeptides in our developmentally regulated gene battery (Fig. 1d and Extended Data Fig. 3) and by their well-known function as modulators of transitions between discrete behavioural states<sup>20,21</sup>. We observed highly neuron-type-specific effects of *lin-4*/*lin-14* on the expression of the analysed genes (Fig. 3a, Extended Data Fig. 9 and Supplementary Table 12). For example, at hatching, the *gfp*-tagged neuropeptide *nlp-45* was primarily expressed in the RIA interneuron but expression was turned on in additional sets of neurons

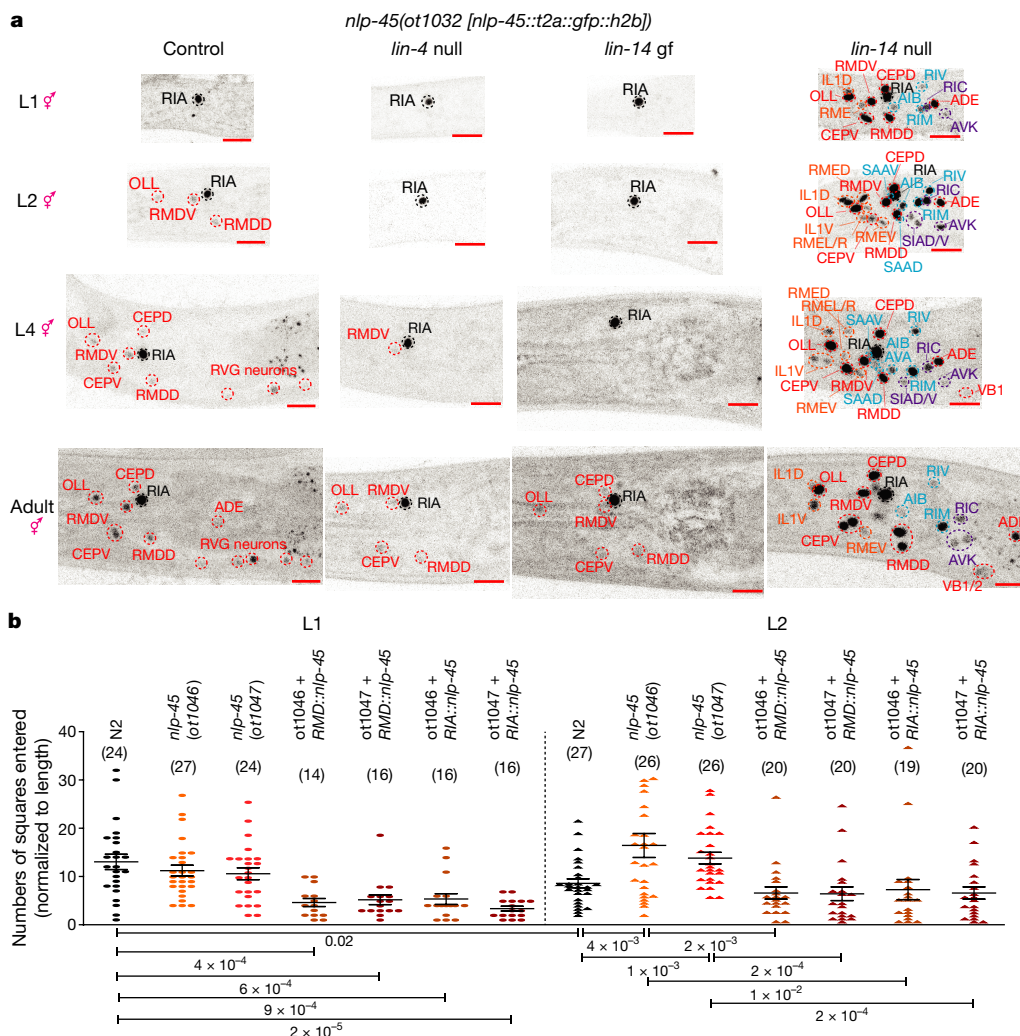


**Fig. 3 | *lin-4* and *lin-14* control developmental changes in exploratory behaviour through regulation of *nlp-45*.** **a**, *nlp-45* expression is juvenized in *lin-4* (*e912*)-null and *lin-14* (*ot1150*)-gain-of-function (gf) animals, whereas more widespread *nlp-45* expression is observed in the *lin-14* (*ma135*)-null mutants, in which neurons that typically express *nlp-45* in the later larval/adult hermaphrodite stage (labelled in red), in adult males (labelled in blue) and in dauer animals (labelled in orange) show expression at the L1 stage. Additional neurons that never show expression in any of the conditions tested (labelled in

purple) also show *nlp-45* expression in *lin-14* (*ma135*)-null animals. Scale bars, 10  $\mu$ m. **b**, *nlp-45* exerts temporally specific effects on exploratory behaviour. Allele and assay details are provided in Extended Data Fig. 10a. The exploratory behaviour is measured as the number of squares entered normalized to the length of the animal. Data are mean  $\pm$  s.e.m. Each point represents a single animal. *n* values are shown in parentheses for each condition. Statistical analysis was performed using two-sided *t*-tests with post hoc corrections; *P* values are shown below.

at subsequent development-stage transitions (Fig. 3a and Extended Data Fig. 3b). In the *lin-4*-null mutant, we observed a ‘juvenized’ pattern of *nlp-45* expression as predicted by our transcriptome profiling experiment: expression remained largely restricted to the RIA interneuron throughout development (Fig. 3a). Similarly, in the *lin-14* (*ot1087*) gain-of-function mutant, we observed a recapitulation of the juvenized expression pattern as observed in the *lin-4*-null mutant (Fig. 3a). By contrast, in the *lin-14* (*ma135*)-null mutant, cells that typically expressed *nlp-45* at later stages showed expression at the L1 stage (Fig. 3a).

Other neuropeptides, as well as the rGC *gcy-12*, revealed *lin-4*/*lin-14*-dependent temporal dynamics of these genes in other individual neuron types (Extended Data Fig. 9b–e and Supplementary Table 12). LIN-14 can act as a repressor on the same gene in some neuronal subtypes and as an activator in another neuronal subtype (Extended Data Fig. 9c), as revealed by *gfp*-tagged neuropeptide *flp-14*. Differential recruitment of additional cofactors may dictate the transcriptional readout of LIN-14 activity.

We used the neuropeptide *nlp-45* as a paradigm to link temporally controlled gene expression changes to changes in animal behaviour.

One of the more dramatic transitions in *nlp-45* expression in hermaphrodites was the transition between L1 and later larval stages, when expression broadened from RIA to additional sets of neurons (Fig. 3a and Extended Data Fig. 3b). One of the locomotor behavioural parameters modulated during this temporal transition was the increased dwelling behaviour of L2 stage animals compared with L1 stage animals (Figs. 1a, 2b, Extended Data Fig. 10a, b and Supplementary Table 1). Two different engineered deletion alleles of *nlp-45* resulted in a stage-specific increase in exploratory behaviour that was observed only in L2, and not L1 stage animals (Fig. 3b and Extended Data Fig. 10a). Transgenic expression of *nlp-45* in either the RMDV or RIA neurons reversed the increased exploratory behaviour of L2 *nlp-45* mutants to that of L2 control (N2) animals (Fig. 3b). The ectopic/overexpression of *nlp-45* in either the RMDV or RIA neurons in L1 stage animals (in which normally only RIA expresses *nlp-45*) further reduced their exploratory behaviour to below that of the L1 controls (Fig. 3b). Consistent with *nlp-45* being a critical effector of the heterochronic pathway, the decreased exploratory behaviour in *lin-14* (*ma135*)-null mutant was partially suppressed in the *nlp-45*-mutant background (Fig. 2c). Together, these data

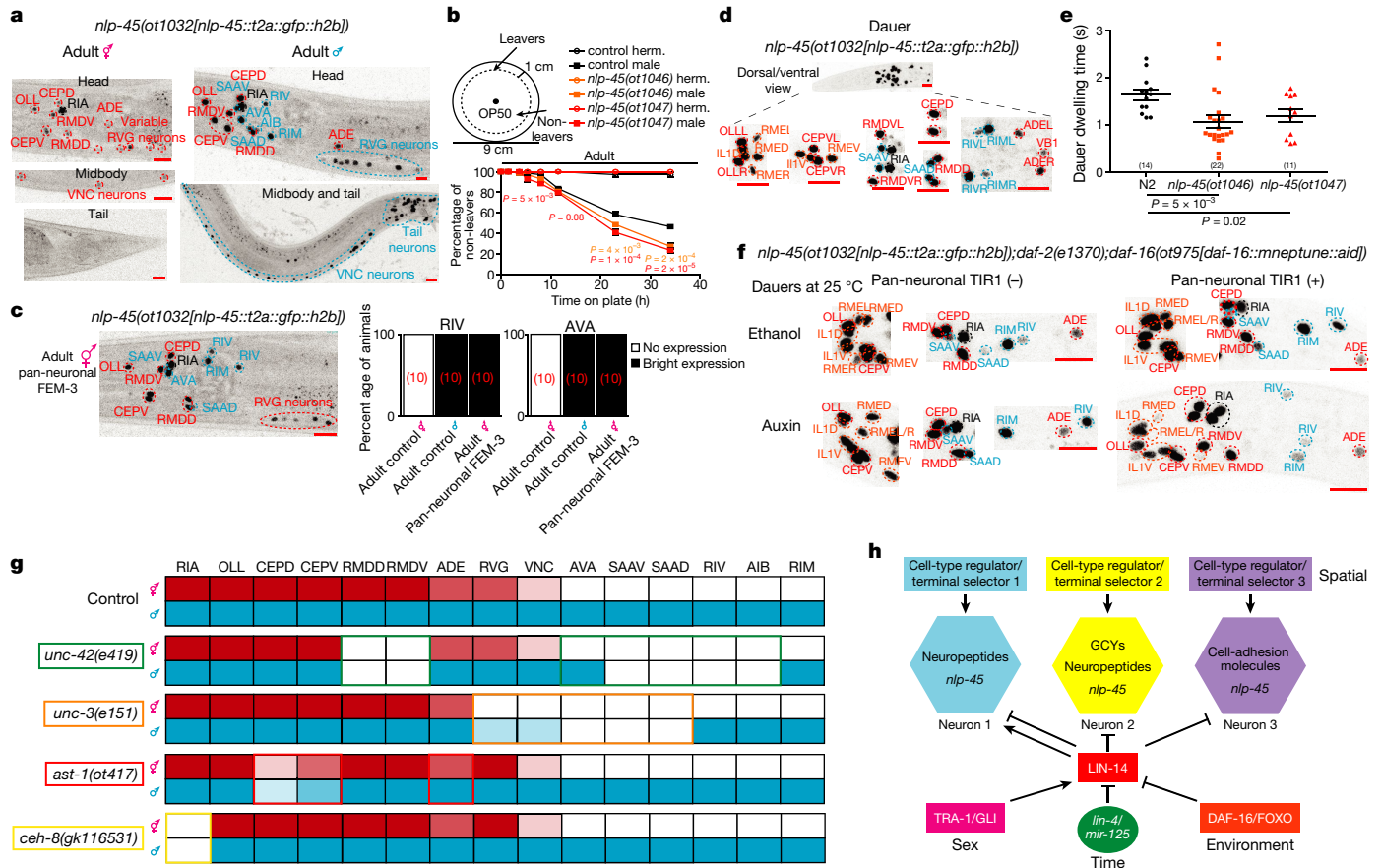


**Fig. 4 | Mechanism of *nlp-45* gene expression regulation across spatial, temporal, sexual and environmental dimensions of post-embryonic development.** **a**, Sexually dimorphic expression of *nlp-45* in adult hermaphrodites (red) and males (blue). **b**, *nlp-45*-deletion mutants show increased food-leaving behaviour in adult males but not in adult hermaphrodites (herm.); the leaving assay was performed as described previously<sup>23</sup>. Data are mean  $\pm$  s.e.m. of three independent experiments for adult hermaphrodites and six independent experiments for adult males.  $n = 12$  animals per independent experiments. Statistical analysis, which was performed using two-sided *t*-tests with post hoc corrections, is shown for only the comparison between *nlp-45*-mutant adult males and control males (*nlp-45*(*ot1046*) versus N2 adult males (orange); *nlp-45*(*ot1047*) versus N2 adult males (red)). **c**, The pan-neuronal depletion of sex determination master regulator TRA-1 through the overexpression of FEM-3 masculinizes *nlp-45* expression in the head of adult hermaphrodites. **d**, After entry into the dauer stage, *nlp-45* expression is observed in neurons that express *nlp-45* normally only in adult males (blue) and

in additional neurons (orange). **e**, *nlp-45*-deletion mutant dauers exhibit reduced dwelling behaviour compared with N2 dauers. Data are mean  $\pm$  s.e.m. Each point represents a single animal.  $n$  values are shown in parentheses for each condition. Statistical analysis was performed using two-sided *t*-tests with post hoc corrections;  $P$  values are shown below. **f**, Pan-neuronal degradation of DAF-16 in auxin-treated dauers leads to a loss of or reduction in *nlp-45* expression in several neurons. Representative images are shown, and quantifications are provided in Extended Data Fig. 10o. **g**, *nlp-45* expression patterns for adult hermaphrodites (red) and males (blue) are shown for control and terminal selector mutant animals. Expression patterns of terminal selectors are shown by their respective coloured outlines. The dimmer red and blue colours represent lower and/or variable *nlp-45* expression, whereas blank boxes represent no expression. Further details are provided in Extended Data Fig. 11a–d. **h**, Schematic of the temporal, sexual and environmental regulation of heterochronic regulator *lin-14*, in combination with cell-specific terminal selectors to dictate spatiotemporal gene batteries. GCY, guanylyl cyclase. Scale bars, 10  $\mu$ m.

suggest that NLP-45 functions as an anti-exploratory neuropeptide that is regulated by the heterochronic pathway during the L1-to-L2 developmental transition (Extended Data Fig. 10c).

We examined two other notable transitions in *C. elegans* post-embryonic development with reported changes in exploratory behaviour. One is the increased, sex-specific exploratory drive of adult males for mate searching over food, which is observed after sexual maturation and is mediated by the PDF-1 neuropeptide<sup>22,23</sup>. Consistent with an involvement of *nlp-45*, there are striking sexual dimorphisms in *nlp-45* expression. In adult males, *nlp-45* was activated in five classes of neurons in the head (SAAD/V, AVA, RIV, AIB, RIM), most retrovesicular ganglion neurons and most ventral nerve cord (VNC) motor neurons, as well as a number of tail neurons (Fig. 4a). This upregulation controlled food-leaving behaviour as *nlp-45*-mutant adult males (but not juveniles or adult hermaphrodites) left food faster/earlier compared with control adult males (Fig. 4b and Extended Data Fig. 10d). Moreover,

the upregulation of *nlp-45* in adult males served as a counterbalancing anti-exploratory signal to the increased exploration drive mediated by *pdf-1* (Extended Data Fig. 10e–g).

We noted that *nlp-45* expression of the early larval *lin-14*(*ma135*)-mutant hermaphrodites largely mimicked that of the wild-type adult males, entailing expression in neurons that was observed only in control adult males (for example, SAAD/V, RIV, AIB, RIM) and also stronger expression in other neuron classes (such as OLL, RMDD/V, CEPD/V) (Figs. 3a and 4a). This observation prompted us to investigate whether the LIN-14 transcription factor is expressed in a sexually dimorphic manner. We indeed found that, although *lin-14* expression was similarly downregulated in both sexes at early larval stages, expression in the L4 stage and, particularly, in the adult stage was significantly more reduced in the male nervous system compared with that of the hermaphrodite (Extended Data Fig. 10h, i). Together, these data indicate that the LIN-14 transcription factor maintained a juvenile *nlp-45* expression pattern by

repressing it in specific neuron classes. The further downregulation of *lin-14* in the adult male nervous system allowed for the derepression of *nlp-45* in other neurons such as SAAD/V, RIV, AIB and RIM.

As ChIP-seq analysis revealed binding of the hermaphrodite-enriched master regulator of sexual identity, TRA-1, to *cis*-regulatory regions of *lin-14* (ref. 24), we examined the effect of TRA-1 on *lin-14* expression. To this end, we eliminated TRA-1 from the nervous system through pan-neuronal overexpression of FEM-3, a negative regulator of TRA-1 expression; overexpression of FEM-3 is frequently used to change the sexual identity of specific cell types<sup>25,26</sup>. We found that, in these animals, *lin-14* expression was significantly reduced in adult hermaphrodites and there was a consequent masculinization of *nlp-45* expression (for example, expression in SAAD/V, AVA, RIV, RIM and VNC motor neurons) (Fig. 4c and Extended Data Fig. 10i, j). In summary, hermaphrodite-enriched *tra-1* expression appears to maintain higher neuronal *lin-14* expression in adult hermaphrodites compared to adult males to prevent the onset of male-specific *nlp-45* expression in specific neuron classes. These observations predict that other LIN-14-dependent genes in hermaphrodites may be expressed in a sexually dimorphic manner as well. Indeed, analysing other reporter-tagged neuropeptide genes, we found this to be the case (Extended Data Fig. 10k–m and Supplementary Table 12).

Another notable example of a developmentally controlled transition in exploratory behaviour is the previously observed increased locomotor quiescence after environmentally induced entry into an alternative developmental stage—the diapause dauer stage<sup>27</sup>. In dauer animals, *nlp-45* gained expression in six classes of head neurons (Fig. 4d). We found that *nlp-45*-mutant dauer animals had reduced dwelling behaviour compared with the control dauer animals (Fig. 4e). Thus, consistent with its anti-exploratory role in early larval stage transitions and after sexual maturation in adult males, *nlp-45* upregulation in dauer animals contributes to the increased locomotor quiescence observed for this stage.

As *nlp-45* expression in *lin-14(ma135)*-null hermaphrodites was observed in neurons that showed only *nlp-45* expression at the dauer stage (for example, RMES, IL1s) (Figs. 3a and 4d), we considered that, similar to the sexually dimorphic regulation of *nlp-45*, environmental regulation of *nlp-45* expression may also converge on the regulation of the transcription factor LIN-14. Indeed, we found that this gain in *nlp-45* expression correlated with a global downregulation of LIN-14 protein in the dauer animals (Extended Data Fig. 10n). Moreover, through neuron-specific removal of *daf-16* (an orthologue of human *FOXO*), the key effector of insulin signalling<sup>27</sup>, we found that this dauer-specific LIN-14 downregulation was cell-autonomously controlled by insulin signalling in the nervous system (Extended Data Fig. 10n). This effect may be direct as ChIP-seq analysis revealed multiple *in vivo* DAF-16-binding sites in the *lin-14 cis*-regulatory region<sup>28</sup>. The derepression of *lin-14* expression observed after neuronal *daf-16* depletion led to the elimination/downregulation of *nlp-45* expression in the six classes of head neurons that gained expression after entry into dauer (Fig. 4f and Extended Data Fig. 10o). The dynamics of *lin-14* expression in the dauer stage predict that other LIN-14-dependent genes may change their expression in the dauer stage. Indeed, analysing other reporter-tagged neuropeptide genes, we found that to be the case (Extended Data Fig. 10p, q and Supplementary Table 12).

To assess how global temporal, sexual and environmental signals result in highly neuron-type-specific modulation of gene (for example, *nlp-45*) expression, we turned to neuron-type-specific transcription factors—terminal selectors, which specify and maintain neuron-type-specific batteries of terminal identity genes<sup>29</sup>. We found that the homeobox gene *unc-42* (an orthologue of human *PROX1*) which controls the differentiation of many *nlp-45*-expressing neurons in both hermaphrodite and male animals<sup>30</sup> is required for *nlp-45* expression in all neurons in which *unc-42* and *nlp-45* expression normally overlap (such as RMDD/V, RIV, SAAD/V), with the exception of AVA, in which *unc-42* acts redundantly with another terminal selector<sup>30</sup> (Fig. 4g and Extended Data Fig. 11a).

Similarly, *unc-3* (an orthologue of human *EBF*), *ast-1* (an orthologue of human *FLII*) and *ceh-8* (an orthologue of human *RAX*) mutants affected *nlp-45* expression in the cell types in which these terminal selectors operate (Fig. 4g and Extended Data Fig. 11b–d).

Terminal selectors and the heterochronic pathway members (that is, *lin-14*) do not regulate one another (Extended Data Fig. 11e, f). Furthermore, *nlp-45* showed precocious expression in *lin-14;unc-42* double mutants, similar to the *lin-14*-null mutant alone, except in the neurons in which *unc-42* acts as a terminal selector (Extended Data Fig. 11g). We conclude that terminal selectors and LIN-14 act in parallel pathways, whereby UNC-42 and other terminal selectors act permissively to promote *nlp-45* expression, but temporal, sexual and dauer signals, integrated on the level of *lin-14* expression, antagonize the ability of UNC-42 to promote *nlp-45* expression (Fig. 4h).

In conclusion, we presented here a comprehensive, nervous-system-wide map of molecular changes that accompany the many behavioural transitions that are associated with the post-embryonic nervous system maturation from juvenile to adult stages of *C. elegans*. Among the most striking changes were those observed in neuropeptidergic signalling. For example, we demonstrated that the spatiotemporal regulation of an anti-exploratory neuropeptide across development resulted in a consequential change in exploratory behaviour across three separate temporal transitions. Consistent with studies in other organisms<sup>21</sup>, our research strongly suggests that neuromodulatory peptides are common regulators of behavioural state transitions across development.

We characterized a genetic program that controls the temporal transitions in neuronal gene expression profiles across post-embryonic development. Studies in vertebrates have focused mostly on the role of environmental stimuli (such as neuronal activity) on the maturation of post-mitotic neuronal features<sup>6,7</sup>, and less attention has been focused on identifying the genetic programs that regulate the temporal identity of post-mitotic neurons, similar to those that have been characterized for the temporal identities of dividing neuroblasts<sup>8–11</sup>. Here we describe how an internal clock—the heterochronic gene pathway, which is composed of several phylogenetically conserved gene regulatory factors—regulates temporal transitions in the expression of many but not all developmentally regulated genes in a highly cell-type-specific manner throughout the nervous system, in apparent collaboration with neuron-type-specific terminal selectors of neuronal identity (Supplementary Discussion). The observation that the sex determination pathway (through the global sex regulator TRA-1) and the environmentally responsive insulin pathway (through DAF-16) regulate LIN-14 expression demonstrates that LIN-14 acts as a key hub to integrate the three different axes of time, sex and environment. ‘Static’ genes are initiated and maintained by neuron-identity-determining terminal selector transcription factors alone, whereas genes dynamically regulated by time, sex or environment depend on both the resident terminal selector of a neuron as well as LIN-14 (Fig. 4h), which either promotes or antagonizes the ability of terminal selectors to activate such target genes.

## Online content

Any methods, additional references, Nature Research reporting summaries, source data, extended data, supplementary information, acknowledgements, peer review information; details of author contributions and competing interests; and statements of data and code availability are available at <https://doi.org/10.1038/s41586-021-04071-4>.

1. Cadwell, C. R., Bhaduri, A., Mostajo-Radji, M. A., Keefe, M. G. & Nowakowski, T. J. Development and arealization of the cerebral cortex. *Neuron* **103**, 980–1004 (2019).
2. Gogtay, N. et al. Dynamic mapping of human cortical development during childhood through early adulthood. *Proc. Natl Acad. Sci. USA* **101**, 8174–8179 (2004).
3. Okaty, B. W., Miller, M. N., Sugino, K., Hempel, C. M. & Nelson, S. B. Transcriptional and electrophysiological maturation of neocortical fast-spiking GABAergic interneurons. *J. Neurosci.* **29**, 7040–7052 (2009).

4. Bakken, T. E. et al. A comprehensive transcriptional map of primate brain development. *Nature* **535**, 367–375 (2016).
5. Kang, H. J. et al. Spatio-temporal transcriptome of the human brain. *Nature* **478**, 483–489 (2011).
6. Spitzer, N. C. Electrical activity in early neuronal development. *Nature* **444**, 707–712 (2006).
7. Stroud, H. et al. An activity-mediated transition in transcription in early postnatal neurons. *Neuron* **107**, 874–890 (2020).
8. Cepko, C. L. The roles of intrinsic and extrinsic cues and bHLH genes in the determination of retinal cell fates. *Curr. Opin. Neurobiol.* **9**, 37–46 (1999).
9. Holguera, I. & Desplan, C. Neuronal specification in space and time. *Science* **362**, 176–180 (2018).
10. Miyares, R. L. & Lee, T. Temporal control of *Drosophila* central nervous system development. *Curr. Opin. Neurobiol.* **56**, 24–32 (2019).
11. Pearson, B. J. & Doe, C. Q. Specification of temporal identity in the developing nervous system. *Annu. Rev. Cell Dev. Biol.* **20**, 619–647 (2004).
12. Witvliet, D. et al. Connectomes across development reveal principles of brain maturation. *Nature* **596**, 257–261 (2021).
13. Yemini, E., Jucikas, T., Grundy, L. J., Brown, A. E. & Schafer, W. R. A database of *Caenorhabditis elegans* behavioral phenotypes. *Nat. Methods* **10**, 877–879 (2013).
14. Steiner, F. A., Talbert, P. B., Kasinathan, S., Deal, R. B. & Henikoff, S. Cell-type-specific nuclei purification from whole animals for genome-wide expression and chromatin profiling. *Genome Res.* **22**, 766–777 (2012).
15. Deal, R. B. & Henikoff, S. A simple method for gene expression and chromatin profiling of individual cell types within a tissue. *Dev. Cell* **18**, 1030–1040 (2010).
16. Ambros, V. & Horvitz, H. R. Heterochronic mutants of the nematode *Caenorhabditis elegans*. *Science* **226**, 409–416 (1984).
17. Rougvie, A. E. & Moss, E. G. Developmental transitions in *C. elegans* larval stages. *Curr. Top. Dev. Biol.* **105**, 153–180 (2013).
18. Feinbaum, R. & Ambros, V. The timing of *lin-4* RNA accumulation controls the timing of postembryonic developmental events in *Caenorhabditis elegans*. *Dev. Biol.* **210**, 87–95 (1999).
19. Ruvkun, G. & Giusto, J. The *Caenorhabditis elegans* heterochronic gene *lin-14* encodes a nuclear protein that forms a temporal developmental switch. *Nature* **338**, 313–319 (1989).
20. Marder, E. Neuromodulation of neuronal circuits: back to the future. *Neuron* **76**, 1–11 (2012).
21. Schoofs, L. & Beets, I. Neuropeptides control life-phase transitions. *Proc. Natl Acad. Sci. USA* **110**, 7973–7974 (2013).
22. Barrios, A., Ghosh, R., Fang, C., Emmons, S. W. & Barr, M. M. PDF-1 neuropeptide signaling modulates a neural circuit for mate-searching behavior in *C. elegans*. *Nat. Neurosci.* **15**, 1675–1682 (2012).
23. Lipton, J., Kleemann, G., Ghosh, R., Lints, R. & Emmons, S. W. Mate searching in *Caenorhabditis elegans*: a genetic model for sex drive in a simple invertebrate. *J. Neurosci.* **24**, 7427–7434 (2004).
24. Berkseth, M., Ikegami, K., Arur, S., Lieb, J. D. & Zarkower, D. TRA-1 CHIP-seq reveals regulators of sexual differentiation and multilevel feedback in nematode sex determination. *Proc. Natl Acad. Sci. USA* **110**, 16033–16038 (2013).
25. Oren-Suissa, M., Bayer, E. A. & Hobert, O. Sex-specific pruning of neuronal synapses in *Caenorhabditis elegans*. *Nature* **533**, 206–211 (2016).
26. Lee, K. & Portman, D. S. Neural sex modifies the function of a *C. elegans* sensory circuit. *Curr. Biol.* **17**, 1858–1863 (2007).
27. Fielenbach, N. & Antebi, A. *C. elegans* dauer formation and the molecular basis of plasticity. *Genes Dev.* **22**, 2149–2165 (2008).
28. Kumar, N. et al. Genome-wide endogenous DAF-16/FOXO recruitment dynamics during lowered insulin signalling in *C. elegans*. *Oncotarget* **6**, 41418–41433 (2015).
29. Hobert, O. Terminal selectors of neuronal identity. *Curr. Top. Dev. Biol.* **116**, 455–475 (2016).
30. Berghoff, E. G. et al. The Prop1-like homeobox gene *unc-42* specifies the identity of synaptically connected neurons. *eLife* **10**, e64903 (2021).

**Publisher's note** Springer Nature remains neutral with regard to jurisdictional claims in published maps and institutional affiliations.

© The Author(s), under exclusive licence to Springer Nature Limited 2021

## Methods

**C. elegans strains and handling**

Worms were grown at 20 °C on nematode growth medium (NGM) plates seeded with *Escherichia coli* (OP50) bacteria as a food source unless otherwise mentioned. Worms were maintained according to the standard protocol. The wild-type strain used was the Bristol variety, strain N2. A complete list of strains and transgenes used in this study is provided in Supplementary Table 13. Whenever synchronization of developmental stages was necessary, animals were egg prepped according to the standard protocol and synchronized at the L1 stage. They were then plated on food and collected after 8 ± 1 h, 21 ± 1 h, 30 ± 2 h, 40 ± 2 h and 53 ± 2 h for the L1, L2, L3, L4 and adult stages, respectively, for either molecular or behavioural analysis. These time points were chosen such that the animals were in the middle of each larval stage or relatively early in adulthood for the analysis. Dauer animals were obtained using standard crowding, starvation and high-temperature conditions.

**Constructs cloning and stain generation**

**UPN::INTACT.** To generate the UPN::INTACT tag (*npp-9::mcherry::3xflag*), a concatenated pan-neuronal promoter<sup>31</sup>, containing promoter fragments from *unc-11*, *rgef-1*, *ehs-1* and *ric-19*, and the INTACT tag<sup>14</sup> were cloned together using Gibson assembly. The construct was injected (5 ng μl<sup>-1</sup> with 100 ng μl<sup>-1</sup> digested OP50 DNA) and the resulting extrachromosomal array strain was integrated into the genome using standard ultraviolet irradiation methods. This was followed by six rounds of backcrossing to N2 to generate *otIs790*.

**Fosmid recombineering.** To generate the *lin-4* fosmid reporter, a standard fosmid recombineering protocol was used as described previously<sup>32</sup>. In brief, a 90 bp *lin-4* primary miRNA was replaced with *nls::yfp::h2b* in fosmid WRM0613aD08. The recombineered fosmid was injected (15 ng μl<sup>-1</sup> with 100 ng μl<sup>-1</sup> digested OP50 DNA), and the resulting extrachromosomal array strain was integrated into the genome using standard ultraviolet irradiation methods. This was followed by two rounds of backcrossing to N2 to generate *otIs763*.

**Genome engineering using CRISPR-Cas9.** *lin-14* (*ot1087/1149/1150/1151*), *lin-28* (*ot1153/1154/1155*), *nlp-45* (*ot1032* [*nlp-45::t2a::gfp::h2b*]), *nlp-45* (*ot1046*) and *nlp-45* (*ot1047*) were generated using Cas9 protein, tracrRNA and crRNAs from IDT, as previously described<sup>33</sup>. For *lin-14* (*ot1087/1149/1150/1151*), two crRNAs (GTTCTGAGA GCAATTTTGG and CAAACTCACAACCAACTCA) and a single-stranded oligodeoxynucleotide (ssODN) donor (TTGCTTTTCTGCTCACTT TACCTTTGTCTCACTTTTCTTACTTCTGTATCACA AAAATGATATA) was used to ensure a precise 466 bp deletion in the *lin-14* 3' UTR to remove all seven LIN-4-binding sites. For *lin-28* (*ot1153/1154/1155*), one crRNA (CCTGAGAGTGCATTTGAGG) and a ssODN donor (CCC CTCTAAACCATACTACCACCTACCTCCTCAAACCTTTTTTTTTTCAAATA GAACTGATTGCACCTGTT) were used to ensure a precise 18 bp deletion in the *lin-28* 3' UTR to remove the single LIN-4-binding site. For *nlp-45* (*ot1032* [*nlp-45::t2a::gfp::h2b*]), two crRNAs (AAGCATCTGGACT GCCGATG and TGA CTTGAACAGGAAGCATC) and an asymmetric double-stranded *t2a::gfp::h2b*, PCR amplified from pBALU43, were used to insert the fluorescent tag at the C terminal. For *nlp-45* (*ot1046*) and *nlp-45* (*ot1047*), two crRNAs (ACTTGCGTTAACCACAATGA and TGA CTTGAACAGGAAGCATC) were used, and random deletions were screened to obtain *nlp-45* (*ot1046*) and *nlp-45* (*ot1047*). These deletions were 43 bp and 239 bp within the first exon, respectively, and both resulted in frameshift mutations and premature stop codons. Neither mutation resulted in the production of the predicted mature peptide (Extended Data Fig. 10a). *npr-17* (*ot1101*) was generated using a standard method as previously described to insert C-terminally fused *gfp*<sup>34</sup>. *ins-6* (*syb2685*), *ins-9* (*syb2616*), *nlp-50* (*syb2704*), *nlp-13* (*syb3411*), *flp-26* (*syb3588*), *flp-28* (*syb3207*) and *flp-14* (*syb3323*) were generated by

SUNY Biotech. To facilitate the neuronal identification of the secreted neuropeptide expression reporters, a nuclear-localized *gfp* was inserted behind the neuropeptide-coding sequences, separated by a T2A sequence that splits the two proteins<sup>35</sup>.

**Single-copy insertion by MiniMos.** The concatenated pan-neuronal promoter (*UPN*) and a 338 bp fragment containing the *lin-4* miRNA were fused together and cloned into pCFJ910 using Gibson Assembly. The plasmid was injected to obtain a single-copy insertion of *UPN::lin-4* as previously described<sup>36</sup>.

**Cell-specific *nlp-45* overexpression.** The *mgl-1* promoter<sup>37</sup> and *glr-3* promoter<sup>38</sup> were PCR amplified from genomic DNA for neuron-specific expression in RMDD/V and RIA neurons, respectively. *nlp-45* cDNA was obtained from Dharmacon. The promoter fragments and the *nlp-45* cDNA were fused together with *sl2::2xnl::tagrfp::p10* 3' UTR by Gibson assembly. The constructs were injected at 50 ng μl<sup>-1</sup> and extrachromosomal array lines were selected according to the standard protocol.

**All other strains.** The *inx-19* fosmid (*otIs773*) was obtained through integration of a previously published extrachromosomal array strain<sup>39</sup>. The *gcy-12* promoter fusion GFP reporter was obtained through integration of an existing extrachromosomal array strain, DA1266. All other strains were previously published, and/or obtained from CGC and/or crosses with these strains as detailed in Supplementary Table 13.

**Neuron identification**

For neuronal cell identification, colocalization with the NeuroPAL landmark strain (*otIs669* or *otIs696*) was used to determine the identity of all neuronal expression as previously described<sup>31</sup>. Examples of how this was carried out are shown in Supplementary Fig. 1. All images for which NeuroPAL was used for identification were deposited in the Zenodo database (<https://zenodo.org/communities/neuropal>).

**Behavioural analysis**

**Automated worm tracking.** Automated single-worm tracking was performed using the Wormtracker 2.0 system at room temperature<sup>13</sup>. Animals at all stages were recorded for 5 min each, except for dauers, which were recorded for 10 min to ensure adequate sampling of locomotor features due to increased quiescence. All animals were tracked on NGM plates that were uniformly covered with food (OP50), except for dauer animals, which were tracked on non-coated plates. Analysis of the tracking videos was performed as previously described<sup>13</sup>.

**Exploratory assay.** To explore exploration behaviour, an adapted exploratory assay from a previous study<sup>40</sup> was used to increase the sensitivity for younger/smaller animals. Individual animals at the respective developmental stages and genotypes were picked onto a 5 cm agar plate uniformly seeded with *E. coli* strain OP50. After 90 min, the plates were superimposed onto a grid containing 1 mm squares, and the number of squares entered by the worm tracks was manually counted. The number of squares explored was adjusted for the length of the animal, to compensate for the different size of animals at different developmental stages/genotypes. Transgenic and mutant strains were always compared with control animals assayed in parallel. All plates were scored by an investigator who was blinded to the genotype of the animals.

**Food-leaving assay.** The food-leaving (also known as mate-searching) assay was performed as previously described<sup>23</sup>. A single drop (18 μl) of OP50 was seeded the day before and allowed to grow. The next day, a single animal of the respective developmental stage, sex and genotype was placed into the centre of a 9 cm agar plate, and each animal that had left the food was scored in a blinded manner at eight time points for a period of up to 55 h. A worm was considered to be a leaver if it was 1 cm from the edge of the plate.

## Microscopy

Worms were anaesthetized using 100 mM of sodium azide and mounted on 5% agarose on glass slides. All images were acquired using a Zeiss confocal microscope (LSM880). Image reconstructions were performed using Zen software tools. Maximum intensity projections of representative images were shown. Fluorescence intensity was quantified using the Zen software. Figures were prepared using Adobe Photoshop and Illustrator.

## INTACT for purification of affinity-tagged neuronal nuclei

UPN::INTACT control worms (*otIs790*) as well as mutants were grown on large plates (150 mm) with enriched peptone medium and coated with NA22 bacteria to allow for the growth of large quantities of worms: 100,000 worms can grow from synchronized L1 stage to gravid adults on a single plate. The animals were collected at the respective stage as described above. *lin-4(e912)* and *lin-14(ot1149)* animals were slower in their developmental progression compared with the controls<sup>41</sup>, and adult *lin-4(e912)* and *lin-14(ot1149)* animals were collected at around  $57 \pm 2$  h (4 h after the control and *lin-28(ot1154)* adult animals were collected). Around 600,000 animals were collected for each L1/L2 replicate, whereas ~200,000 animals were collected for each L4/adult replicate. At the time of collection, animals were washed off the plate with M9, washed three times with M9, lightly fixed with cold RNase-free *N,N*-dimethylformamide (DMF, Sigma D4551) for 2 min before washing three times with 1× PBS.

Modifications were made from the previous INTACT protocol<sup>14,15</sup> to optimize the pull-down of neuronal nuclei. All of the following steps were performed in cold rooms (4 °C) to minimize the degradation of the RNA and protein tag. The animals were homogenized mechanically using disposable tissue grinders (Thermo Fisher Scientific) in 1× hypotonic buffer (1× HB: 10 mM Tris pH 7.5, 10 mM NaCl, 10 mM KCl, 2 mM EDTA, 0.5 mM EGTA, 0.5 mM spermidine, 0.2 mM spermine, 0.2 mM dithiothreitol, 0.1% Triton X-100 and 1× protease inhibitor). After each round of mechanical grinding (60 turns of the grinder), the grinder was washed with 1 ml 1× HB and the entire homogenate was centrifuged at 100g for 3 min. The supernatant was collected for later nuclei extraction and the pellet was put under mechanical grinding and centrifugation for four additional rounds. The supernatants collected from each round were pooled, dounced in a glass dounce and gently passed through an 18-gauge needle twenty times to further break down small clumps of cells. The supernatant was then centrifuged at 100g for 10 min to further remove debris and large clumps of cells. Nuclei were isolated from the supernatant using Optiprep (Sigma-Aldrich): after centrifugation, the supernatant was collected in a 50 ml tube, with added nuclei purification buffer (1× NPB: 10 mM Tris pH 7.5, 40 mM NaCl, 90 mM KCl, 2 mM EDTA, 0.5 mM EGTA, 0.5 mM spermidine, 0.2 mM spermine, 0.2 mM dithiothreitol, 0.1% Triton X-100 and 1× protease inhibitor) to 20 ml, and layered on top of 5 ml of 100% Optiprep and 10 ml of 40% Optiprep. The layered solution was centrifuged at 5,000g for 10 min in a swinging-bucket centrifuge at 4 °C. The nuclei fraction was collected at the 40/100% Optiprep interface. After removing the top and bottom layers, leaving a small volume containing the nuclei, the process was repeated two more times. After the final collection of the crude nuclei fraction, the volume was added to 4 ml with 1× NPB and precleared with 10 µl of Protein G Dynabeads and 10 µl of M270 carboxylated beads for 30 min to 1 h (Invitrogen). The precleared nucleus extract was then removed, and 50 µl was taken out as input samples (total nuclei). The rest was incubated with 30 µl of Protein G Dynabeads and 3 µl of anti-Flag M2 antibodies (Sigma-Aldrich) overnight to immunoprecipitate (IP) the neuronal nuclei. The next day, the immunoprecipitated neuronal nuclei/beads were washed 6–8 times with 1× NPB for 10–15 min each time. The resulting immunoprecipitated neuronal nuclei/beads were resuspended in 50 µl 1× NPB, and a small aliquot was used to check

with DAPI staining to quality-check the procedure for the following: (1) sufficient quantities of nuclei were immunoprecipitated; (2) nuclei were intact and not broken; and (3) the majority of bound nuclei were single, mCherry-labelled neuronal nuclei, and minimal nuclei clumps and large tissue chunks were immunoprecipitated. Samples that did not satisfy these quality checks were not used for downstream processing. The resulting input and neuronal IP samples were used for isolation of total RNA using the Nucleospin RNA XS kit according to the manufacturer's protocol (Takara).

## RNA-seq and data analysis

RNA-seq libraries were prepared using the Universal RNA-seq kit (Tecan) according to the manufacturer's protocol. The libraries were sequenced on Illumina NextSeq 500 machines with 75 bp single-end reads. After the initial quality check, the reads were mapped to WS220 using the Sub-read package<sup>42</sup>, and assigned to genes using featurecounts. Neuronal enrichment was conducted by comparing neuronal IP samples to their respective input samples using DESeq2, with batch effect taken into account for the analysis<sup>43</sup>. We found that 7,974 genes were neuronally enriched (Supplementary Table 2). We took the read counts of these 7,974 genes for all of the IP samples across development, normalized for library size, and conducted all developmental and mutant analysis using DESeq2. We found that this approach minimized contamination artifacts resulting from the protocol and led to the best biological validation.

## ChIP-seq and analysis

The C-terminally GFP-tagged *lin-14* (*lin14(cc2841[lin-14::gfp])*) and N2 strains were used for the ChIP analysis. Around 600,000 animals were collected for each L1/L2 replicate and fixed with 2% formaldehyde for 15 min at room temperature. ChIP assays were performed as previously described with the following modifications<sup>44</sup>. After fixation, worms were resuspended in FA buffer supplemented with protease inhibitors (150 mM NaCl, 10 µl of 0.1 M phenylmethylsulfonyl fluoride, 100 µl 10% SDS, 500 µl 20% *N*-lauroyl sarcosine sodium, 1 cOmplete ULTRA Protease Inhibitor Cocktail tablet in 10 ml FA buffer). The sample was sonicated using a Covaris S220 system at the following settings: 200 W peak incident power, 20% duty factor, 200 cycles per burst for 6 min. The samples were transferred to centrifuge tubes and centrifuged at the highest speed for 15 min. The supernatant was transferred to a new tube, and 5% of the material was saved as the input. The remainder was incubated with 25 µl GFP-Trap Magnetic Beads (Chromotek) at 4 °C overnight. Wild-type (N2) worms without the GFP tag were used as a negative control. The next day, the beads were washed at 4 °C twice with 150 mM NaCl FA buffer (5 min each), once with 1 M NaCl FA buffer (5 min), twice with 500 mM NaCl FA buffer (10 min each), once with TEL buffer (0.25 M LiCl, 1% NP-40, 1% sodium deoxycholate, 1 mM EDTA, 10 mM Tris-HCl, pH 8.0) for 10 min and twice with TE buffer (5 min each). The immunocomplex was then eluted in 200 µl elution buffer (1% SDS in TE with 250 mM NaCl) by incubating at 65 °C for 20 min. The input and ChIP samples were then treated with 1 µl of 20 mg ml<sup>-1</sup> proteinase K, incubated at 55 °C for 2 h, and then at 65 °C overnight to reverse cross-link. The immunoprecipitated DNA was purified using Ampure XP beads (A63881) according to the manufacturer's instructions, and used to generate sequencing library using Ovation Ultralow System V2 (Tecan) according to the manufacturer's instructions. The libraries were sequenced on Illumina NextSeq 500 machines with 75 bp single-end reads. After initial quality check, the reads were mapped to WS220 using BWA<sup>45</sup> and filtered using SAMtools<sup>46</sup>. Peaks were called using MACS2 (ref. <sup>47</sup>). The ChIP-seq peak distribution was calculated and plotted using ChIPseeker<sup>48</sup>. The consensus binding motif was obtained using MEME-ChIP<sup>49</sup>. Differential binding analysis between L1 and L2 was performed using Diffbind<sup>50</sup>. All peaks and differential binding sites were annotated and assigned to the nearest gene using ChIPseeker<sup>48</sup>.

## Auxin-inducible degradation

The AID system was used as previously described<sup>39,51</sup>. The conditional *daf-16* allele *daf-16(ot975[daf-16::mneptune2.5::3xflag::aid])<sup>52</sup>* was crossed with *daf-2(e1370)*, pan-neuronal TIR1-expressing transgenic lines and *lin-14/nlp-45* reporters to generate the experimental strains. Animals were grown (from embryo onwards) on NGM plates supplemented with OP50 and 4 mM auxin in ethanol (indole-3 acetic acid, Alfa Aesar) at 25 °C to degrade DAF-16 pan-neuronally and to induce dauer formation. As controls, plates were supplemented with the solvent ethanol instead of auxin. Additional control animals without pan-neuronal TIR-1 expression grown on ethanol and auxin were also included for comparison.

## Quantification, statistical analysis and reproducibility

Statistical analysis of the automated worm tracking videos was performed as previously described<sup>13</sup>. In brief, statistical significance between each group was calculated in a blinded manner using Wilcoxon rank-sum tests and correcting for false-discovery rate. Statistical analysis of RNA-seq comparison was performed using DESeq2 as previously described<sup>43</sup>. Statistical analysis of various aspects of ChIP-seq was performed using MACS2, MEME-ChIP and Diffbind<sup>47,49,50</sup>.

All microscopy fluorescence quantifications were performed using Zen software (Carl Zeiss). For image quantification, all direct comparisons were performed in the same imaging sessions with the same laser settings. Wherever possible, an internal control (that is, another fluorescent marker within the same strain) that was not altered by the different experimental conditions was used for normalization. If that was not possible, then the image was normalized to the background fluorescence (taken as the same size box outside of the worm across all conditions).

For all behavioural assays, randomization and blinding was performed wherever possible. For all other molecular and microscopy experiments, experimenters were not blind during data collection/analysis. All statistical tests for fluorescence quantification and behaviour assays were conducted using Prism (GraphPad) and Excel as described in figure legends.

All experiments were repeated at least once independently. At each repeat, all control and experimental conditions were included, and the results of all independent experiments were combined. Whenever representative microscopy images were shown without any quantification, the exact same results were observed in at least ten animals unless variability is stated.

## Reporting summary

Further information on research design is available in the Nature Research Reporting Summary linked to this paper.

## Data availability

Raw and processed RNA-seq data are available under Gene Expression Omnibus (GEO) accession GSE158274. Raw and processed ChIP-seq data are available under GEO accession GSE181288. Raw microscope images of gene expression reporters with NeuroPAL for neuronal cell ID are available at <https://zenodo.org/communities/neuropal>.

31. Yemini, E. et al. NeuroPAL: a multicolor atlas for whole-brain neuronal identification in *C. elegans*. *Cell* **184**, 272–288 (2021).
32. Tursun, B., Cochella, L., Carrera, I. & Hobert, O. A toolkit and robust pipeline for the generation of fosmid-based reporter genes in *C. elegans*. *PLoS ONE* **4**, e4625 (2009).

33. Dokshin, G. A., Ghanta, K. S., Piscopo, K. M. & Mello, C. C. Robust genome editing with short single-stranded and long, partially single-stranded dna donors in *Caenorhabditis elegans*. *Genetics* **210**, 781–787 (2018).
34. Dickinson, D. J., Pani, A. M., Heppert, J. K., Higgins, C. D. & Goldstein, B. Streamlined genome engineering with a self-excising drug selection cassette. *Genetics* **200**, 1035–1049 (2015).
35. Ahier, A. & Jarriault, S. Simultaneous expression of multiple proteins under a single promoter in *Caenorhabditis elegans* via a versatile 2A-based toolkit. *Genetics* **196**, 605–613 (2014).
36. Frokjaer-Jensen, C. et al. Random and targeted transgene insertion in *Caenorhabditis elegans* using a modified Mos1 transposon. *Nat. Methods* **11**, 529–534 (2014).
37. Zhang, F. et al. The LIM and POU homeobox genes *ttx-3* and *unc-86* act as terminal selectors in distinct cholinergic and serotonergic neuron types. *Development* **141**, 422–435 (2014).
38. Brockie, P. J., Madsen, D. M., Zheng, Y., Mellem, J. & Maricq, A. V. Differential expression of glutamate receptor subunits in the nervous system of *Caenorhabditis elegans* and their regulation by the homeodomain protein UNC-42. *J. Neurosci.* **21**, 1510–1522 (2001).
39. Bhattacharya, A., Aghayeva, U., Berghoff, E. G. & Hobert, O. Plasticity of the electrical connectome of *C. elegans*. *Cell* **176**, 1174–1189 (2019).
40. Flavell, S. W. et al. Serotonin and the neuropeptide PDF initiate and extend opposing behavioral states in *C. elegans*. *Cell* **154**, 1023–1035 (2013).
41. Chalfie, M., Horvitz, H. R. & Sulston, J. E. Mutations that lead to reiterations in the cell lineages of *C. elegans*. *Cell* **24**, 59–69 (1981).
42. Liao, Y., Smyth, G. K. & Shi, W. The R package Rsubread is easier, faster, cheaper and better for alignment and quantification of RNA sequencing reads. *Nucleic Acids Res.* **47**, e47 (2019).
43. Love, M. I., Huber, W. & Anders, S. Moderated estimation of fold change and dispersion for RNA-seq data with DESeq2. *Genome Biol.* **15**, 550 (2014).
44. Li, Y. et al. Establishment and maintenance of motor neuron identity via temporal modularity in terminal selector function. *eLife* **9**, e59464 (2020).
45. Li, H. & Durbin, R. Fast and accurate short read alignment with Burrows-Wheeler transform. *Bioinformatics* **25**, 1754–1760 (2009).
46. Li, H. et al. The Sequence Alignment/Map format and SAMtools. *Bioinformatics* **25**, 2078–2079 (2009).
47. Feng, J., Liu, T., Qin, B., Zhang, Y. & Liu, X. S. Identifying ChIP-seq enrichment using MACS. *Nat. Protoc.* **7**, 1728–1740 (2012).
48. Yu, G., Wang, L. G. & He, Q. Y. ChIPseeker: an R/Bioconductor package for ChIP peak annotation, comparison and visualization. *Bioinformatics* **31**, 2382–2383 (2015).
49. Machanick, P. & Bailey, T. L. MEME-ChIP: motif analysis of large DNA datasets. *Bioinformatics* **27**, 1696–1697 (2011).
50. Ross-Innes, C. S. et al. Differential oestrogen receptor binding is associated with clinical outcome in breast cancer. *Nature* **481**, 389–393 (2012).
51. Zhang, L., Ward, J. D., Cheng, Z. & Dernburg, A. F. The auxin-inducible degradation (AID) system enables versatile conditional protein depletion in *C. elegans*. *Development* **142**, 4374–4384 (2015).
52. Aghayeva, U., Bhattacharya, A. & Hobert, O. A panel of fluorophore-tagged *daf-16* alleles. *MicroPubl. Biol.* **2020**, <https://doi.org/10.17912/micropub.biology.000210> (2020).
53. Harris, D. T. & Horvitz, H. R. MAB-10/NAB acts with LIN-29/EGR to regulate terminal differentiation and the transition from larva to adult in *C. elegans*. *Development* **138**, 4051–4062 (2011).
54. Aeschmann, F. et al. LIN41 post-transcriptionally silences mRNAs by two distinct and position-dependent mechanisms. *Mol. Cell* **65**, 476–489 (2017).
55. Ramirez, F. et al. deepTools2: a next generation web server for deep-sequencing data analysis. *Nucleic Acids Res.* **44**, W160–W165 (2016).

**Acknowledgements** We thank Q. Chen and A. Bhattacharya for generating transgenic lines; D. Rahe for help with INTACT optimization; A. Romero and E. Yemini for help with worm tracking; L. Cochella, M. P. Hart, I. Beets and members of the Hobert laboratory for comments on the manuscript; and staff at Wormbase and the CGC for providing resources and reagents. This work was funded by the NIH K99 HD098371, National Research Council of Canada (Holmes Award) and by the Howard Hughes Medical Institute. Some strains were provided by the CGC, which is funded by the NIH Office of Research Infrastructure Program (P40 OLD010440).

**Author contributions** Conceptualization: H.S. and O.H. Methodology: H.S. Validation: H.S. Formal analysis: H.S. Investigation: H.S. Resources: H.S. Writing—original draft: H.S. Writing—review and editing: H.S. and O.H. Visualization: H.S. Supervision: H.S. and O.H. Funding acquisition: H.S. and O.H.

**Competing interests** The authors declare no competing interests.

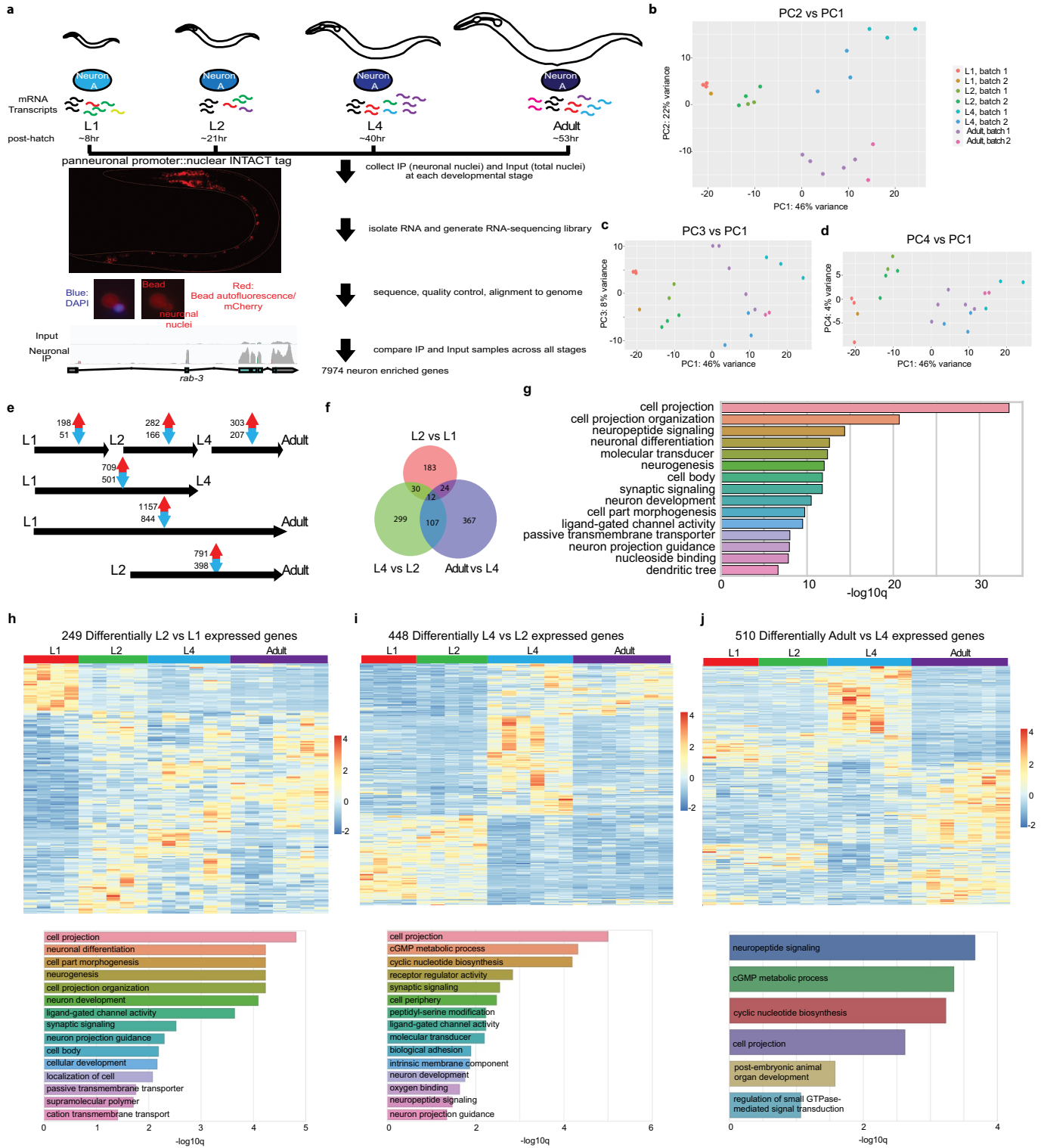
## Additional information

**Supplementary information** The online version contains supplementary material available at <https://doi.org/10.1038/s41586-021-04071-4>.

**Correspondence and requests for materials** should be addressed to HaoSheng Sun or Oliver Hobert.

**Peer review information** Nature thanks Douglas Portman and the other, anonymous, reviewer(s) for their contribution to the peer review of this work. Peer reviewer reports are available.

**Reprints and permissions information** is available at <http://www.nature.com/reprints>.

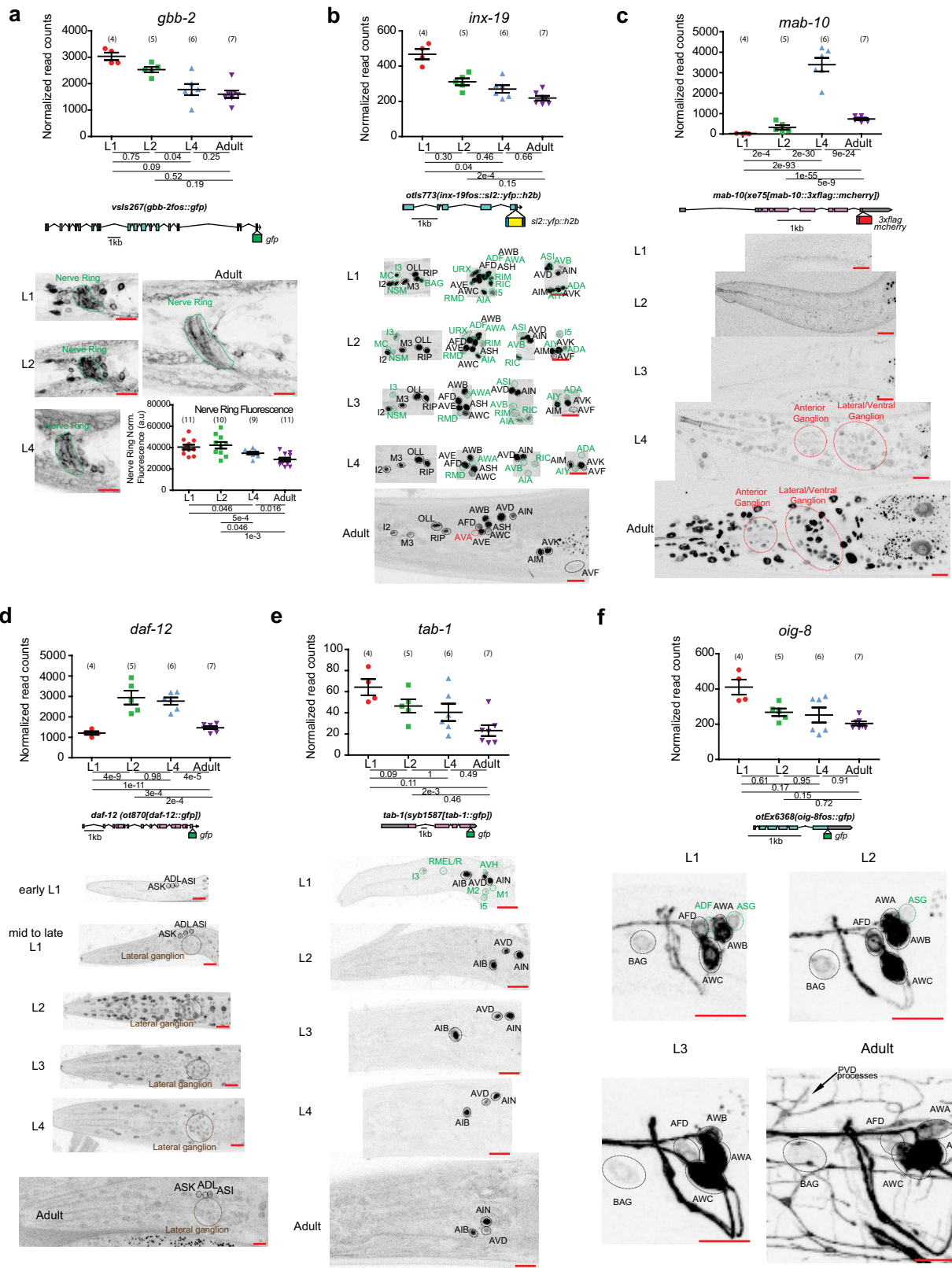


Extended Data Fig. 1 | See next page for caption.

# Article

**Extended Data Fig. 1 | Developmental transitions in neuronal transcriptome across post-embryonic life stages.** **a**, Schematic and experimental design for INTACT sample collection, protocol, and data analysis for neuronal transcriptome profiling across development. Representative images of the pan-neuronal INTACT strain as well as neuronal nuclei after immunoprecipitation (IP) are shown in bottom left panels. Representative tracks from IGV are shown for input and neuronal IP samples to demonstrate IP enrichment for pan-neuronally expressed gene, *rab-3*. **b–d**, Principal component analysis (PCA) of neuronal transcriptome across post-embryonic development was conducted using DESeq2 in R studio<sup>43</sup>. Both batch as well as developmental stage were taken as factors for analysis. Each dot represents a replicate in the RNA-seq analysis. **b**, PC2 vs PC1. PC1 and 2 delineated the transitions between early larval (L1 and L2) stages and late larval (L4)/adult stages, and between all larval (L1 through L4) stages and the adult stage, respectively. **c**, PC3 vs PC1. PC3 largely accounted for variation as a result of batch. **d**, PC4 vs PC1. PC4 largely accounted for L2 specific changes. **e**, The numbers of significant ( $P_{adj} < 0.01$ ) increases/decreases in gene expression are

shown for each stage transition. **f**, Venn diagram of developmental changes in neuronal gene expression across different stage transitions, showing some overlaps but also distinct developmental changes across each stage transition. **g**, Gene ontology analysis of the 2639 developmentally regulated genes using the Enrichment Tool from Wormbase. **h**, Top: heat map of the 249 developmentally regulated genes between L1 and L2 stages across post-embryonic development. In addition to developmentally upregulated and downregulated genes, there was a small subset of genes that showed specific upregulation at the L2 stage. Bottom: gene ontology analysis of these genes using the Enrichment Tool from Wormbase. **i**, Top: heat map of the 448 developmentally regulated genes between L2 and L4 stages across post-embryonic development. Bottom: gene ontology analysis of these genes using the Enrichment Tool from Wormbase. **j**, Top: heat map of the 510 developmentally regulated genes between L4 and adult stages across post-embryonic development. Bottom: gene ontology analysis of these genes using the Enrichment Tool from Wormbase.

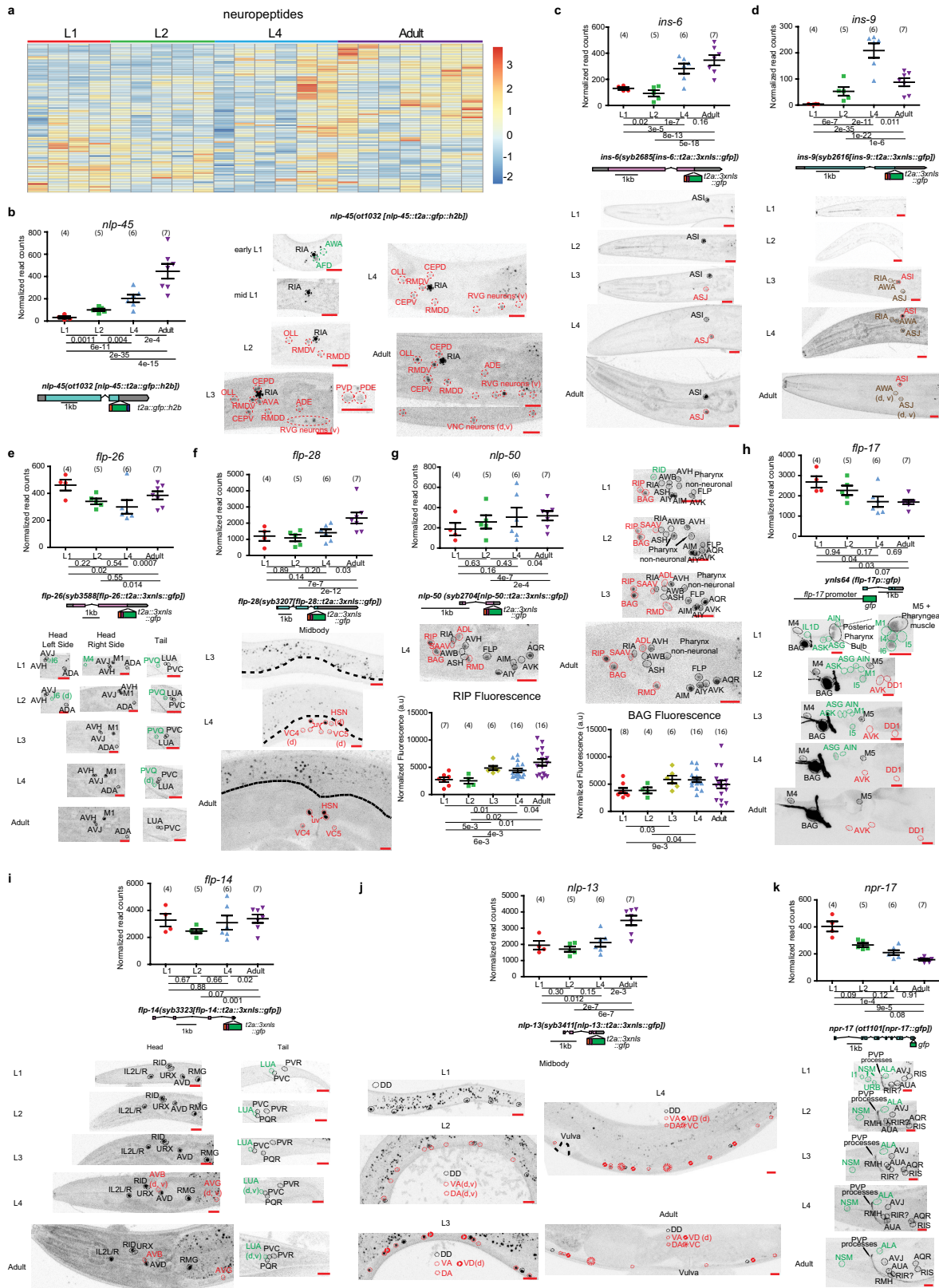


Extended Data Fig. 2 | See next page for caption.

# Article

**Extended Data Fig. 2 | Temporal transitions in nervous system gene expression across *C. elegans* post-embryonic development.** For all panels, validations of developmentally regulated genes with expression reporters are shown. On top are the scattered dot plots (each point represents a single replicate, n in bracket) of the normalized read counts across all developmental stages from the neuronal INTACT/RNA-seq profiling. Mean +/- SEM are shown for each stage. Adjusted *P* values ( $P_{adj}$ ), as calculated by DESeq2, for each developmental comparison are below. Below the RNA-seq read count plots are the schematics and allele names of the expression reporters. Below that are representative confocal microscopy images of the expression reporters across development. Specific regions/neurons are labelled with dotted lines: those labelled with black dotted lines/names are not altered developmentally while those labelled with green and red lines/names demonstrate, respectively, decreases and increases in expression across development. Those labelled with brown lines/names demonstrate both increases and decreases in expression in the same neurons across development. Red scale bars (10µm) are on the bottom right of all representative images. For all panels, L1 through L4 represent the first through the fourth larval stage animals. For **a**, additional quantification of fluorescence intensity is also shown at the bottom. Two-sided t-test with post hoc correction *P* values and n (in bracket) are shown. Additional details are included in Supplementary Table 6. **a**, Metabotropic glutamate receptor *gbb-2*, as validated with a translational fosmid reporter (*gfp*), shows

expression in the same set of neurons across development<sup>31</sup>, although the intensity of expression is decreased across development, including that in the nerve ring as measured with fluorescence intensity. **b**, Gap junction molecule *inx-19*, as validated with a transcriptional fosmid reporter (*sl2::yfp::h2b*), loses expression in sixteen neuronal classes across development and gains expression in the AVA neuron upon entry into adulthood. **c**, Transcription cofactor *mab-10*, as validated with an endogenous translational reporter (*3xflag::mcherry*) engineered with CRISPR/Cas9, gains expression across the nervous system amongst other tissue during transition into the L4 stage that is further upregulated in adulthood. The RNA prediction matches well with previous RNA FISH analysis<sup>53</sup>. The difference between RNA data and protein reporter expression is consistent with previous characterized post-transcriptional regulation by LIN-41<sup>54</sup>. **d**, Nuclear hormone receptor *daf-12*, as validated with an endogenous translational reporter (*gfp*) engineered with CRISPR-Cas9, shows increased expression broadly across the nervous system during early/mid-larval stage and then decreased expression upon transition into late larval/adult stage. **e**, Homeodomain transcription factor *tab-1*, as validated with an endogenous translational reporter (*gfp*) engineered with CRISPR-Cas9, loses expression in five classes of neuron during early larval development. **f**, Immunoglobulin-like domain molecule *oig-8*, as validated with a translational fosmid reporter (*gfp*), loses expression in two classes of neuron during early larval development.

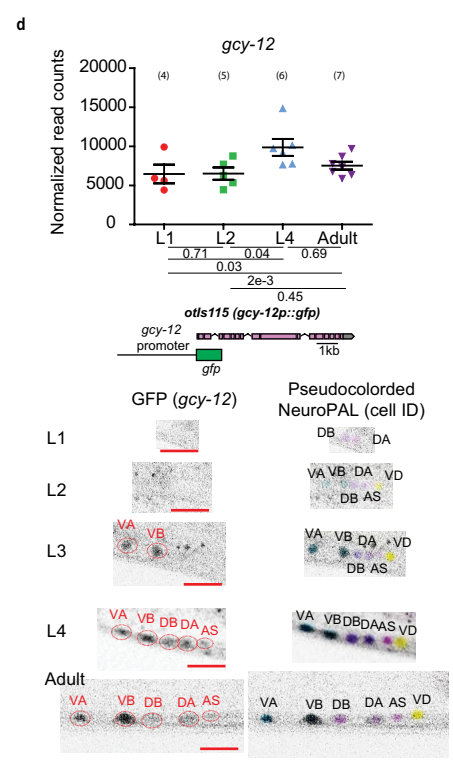
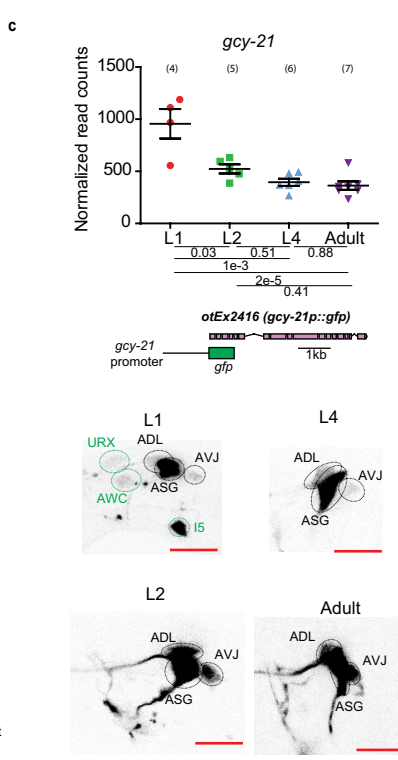
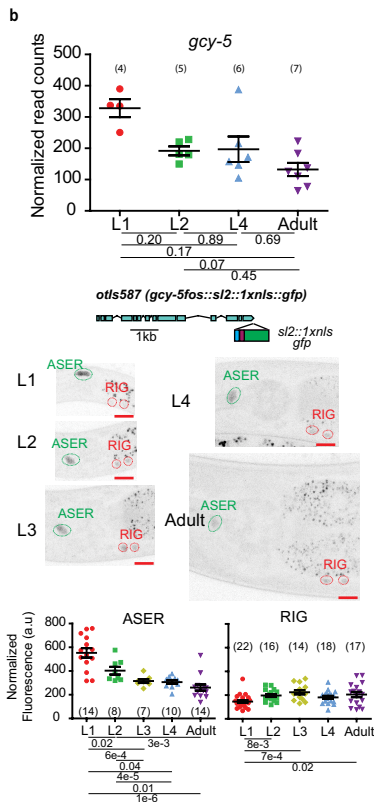
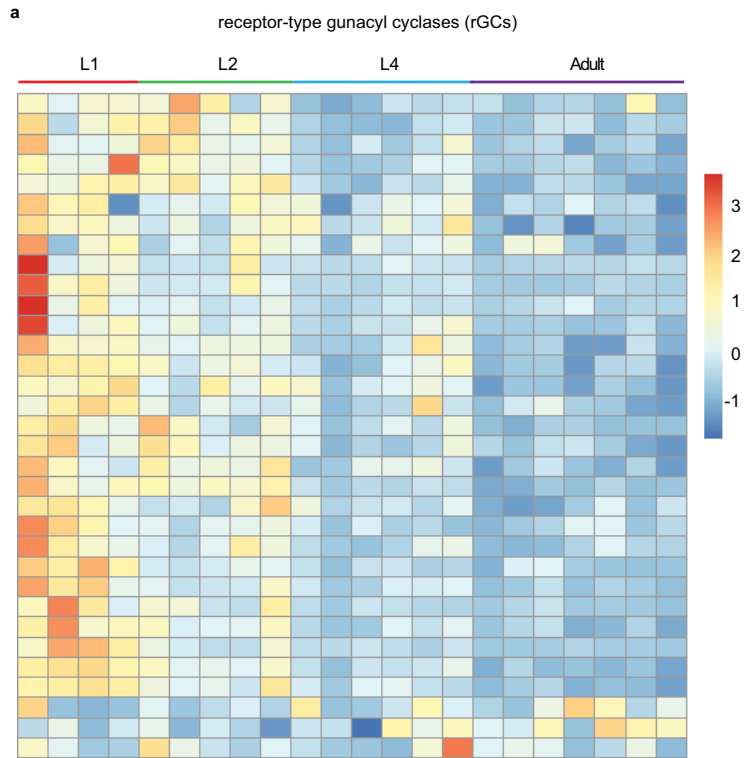


Extended Data Fig. 3 | See next page for caption.

# Article

**Extended Data Fig. 3 | Temporal transitions in nervous system gene expression across *C. elegans* post-embryonic development for the neuropeptide family.** **a**, Heat map of all neuronally enriched neuropeptides across post-embryonic development. Values were z-score normalized and plotted using pheatmap in R studio. Each row represents a single gene, and each column represents a single RNA-seq replicate. For **b–k**, validations of developmentally regulated genes with expression reporters are shown. On top (left for **b**) are the scattered dot plots (each point represents a single replicate, n in bracket) of the normalized read counts across all developmental stages from the neuronal INTACT/RNA-seq profiling. Mean  $\pm$  SEM are shown for each stage. Adjusted *P* values ( $P_{adj}$ ), as calculated by DESeq2, for each developmental comparison are below. Below the RNA-seq read count plots are the schematics and allele names of the expression reporters. Below that (to the right for **b, g**) are representative confocal microscopy images of the expression reporters across development. Specific regions/neurons are labelled with dotted lines: those labelled with black dotted lines/names are not altered developmentally while those labelled with green and red lines/names demonstrate, respectively, decreases and increases in expression across development. Those labelled with brown lines/names demonstrate both increases and decreases in expression in the same neurons across development. d and v in brackets denotes dim and variable expression, respectively. Red scale bars (10  $\mu$ m) are on the bottom right of all representative images. For all panels, L1 through L4 represent the first through the fourth larval stage animals. Additional details are included in Supplementary Table 6. **b**, Other than some remnant expression from embryo in early L1 animals, *nlp-45* gains expression progressively in a number of neurons across development. **c**, Neuropeptide-encoding gene *ins-6*, as validated with an endogenous reporter (*t2a::3xnl::gfp*) engineered with CRISPR-Cas9, gains expression in ASJ across the L2->L3 transition. Variable AWA expression (not shown) is detected in L3 animals onwards. **d**, Neuropeptide-encoding gene *ins-9*, as validated with an endogenous reporter (*t2a::3xnl::gfp*) engineered with CRISPR-Cas9, gains expression in a number of

neurons as it enters L3/L4 stages and loses expression in a subset of these neurons upon entry into adulthood. Extremely variable and dim RVG neuron expression (VBI/2, not shown) is detected in L3/L4 animals. **e**, Neuropeptide-encoding gene *flp-26*, as validated with an endogenous reporter (*t2a::3xnl::gfp*) engineered with CRISPR-Cas9, loses expression in M4 and I6 pharyngeal neurons across early larval development and loses expression in PVQ as it enters late larval/adult stages. **f**, Neuropeptide-encoding gene *flp-28*, as validated with an endogenous reporter (*t2a::3xnl::gfp*) engineered with CRISPR-Cas9, gains expression in hermaphrodite specific neurons (VC, HSN) as it enters late larval/adult stages. Head/tail neurons do not appear to be developmentally regulated in this reporter (images not shown). **g**, Neuropeptide-encoding gene *nlp-50*, as validated with an endogenous reporter (*t2a::3xnl::gfp*) engineered with CRISPR-Cas9, gains expression in a number of neurons across development. It also loses expression in the RID neuron during early larval development. Additional quantification of RIP and BAG fluorescence intensity across development is also shown at the bottom. Two-sided t-test with post hoc correction *P* values and n in brackets are shown. **h**, Neuropeptide-encoding gene *flp-17*, as validated with a promoter fusion reporter (*gfp*), loses and gains expression in nine and two classes of neurons, respectively, across post-embryonic development. **i**, Neuropeptide-encoding gene *flp-14*, as validated with an endogenous reporter (*t2a::3xnl::gfp*) engineered with CRISPR-Cas9, loses and gains expression in one (LUA) and two (AVB and AVG) classes of neurons as it enters late larval/adult stages, respectively. **j**, Neuropeptide-encoding gene *nlp-13*, as validated with an endogenous reporter (*t2a::3xnl::gfp*) engineered with CRISPR-Cas9, gains expression in the ventral nerve cord neurons (DA, VA, VD, VC) across development. Head/tail neurons do not appear to be developmentally regulated in this reporter (images not shown). **k**, Neuropeptide receptor gene *npr-17*, as validated with an endogenous translational reporter (*gfp*) engineered with CRISPR-Cas9, shows decreased and increased expression in four and one classes of neurons, respectively.

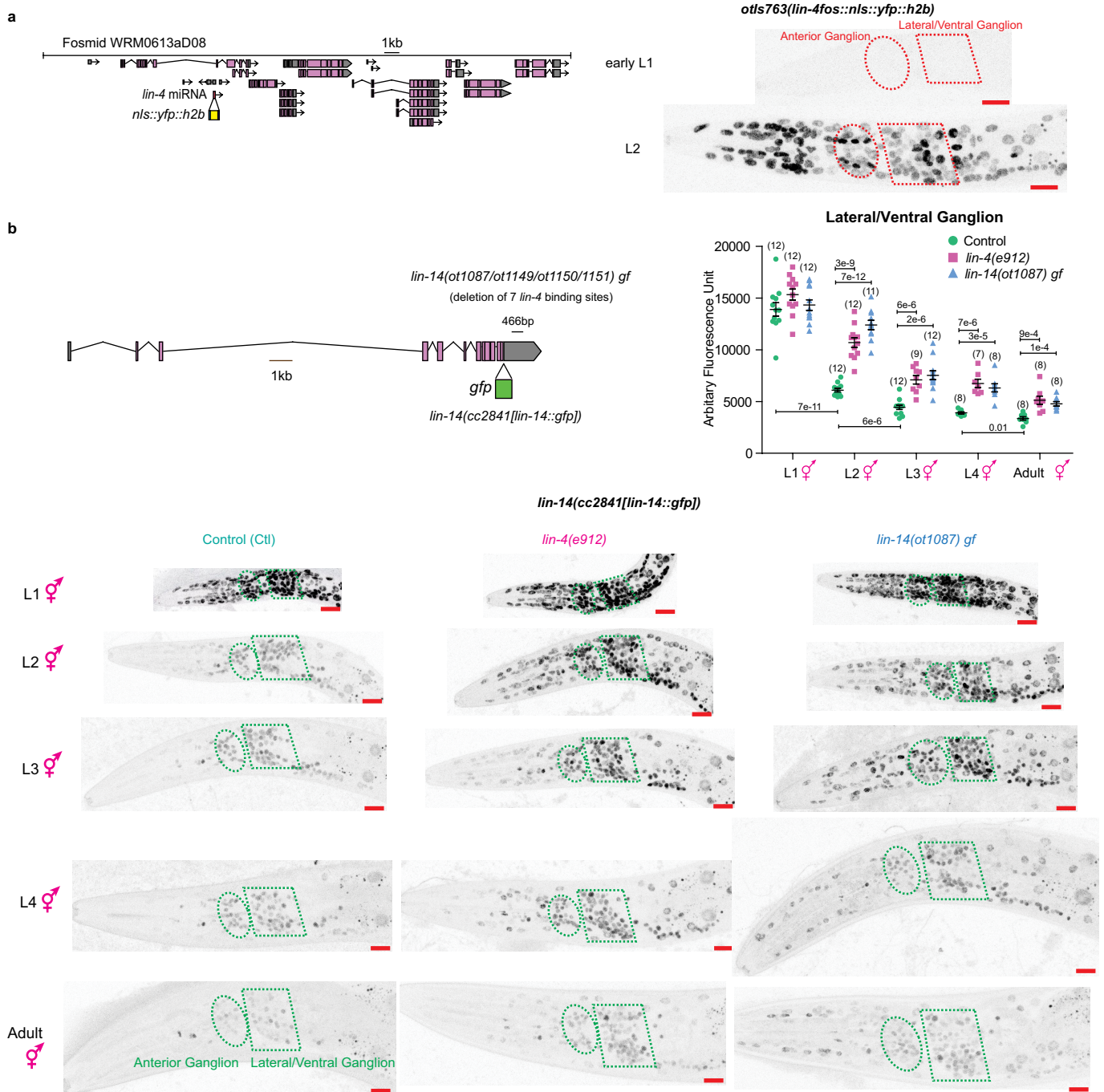


Extended Data Fig. 4 | See next page for caption.

# Article

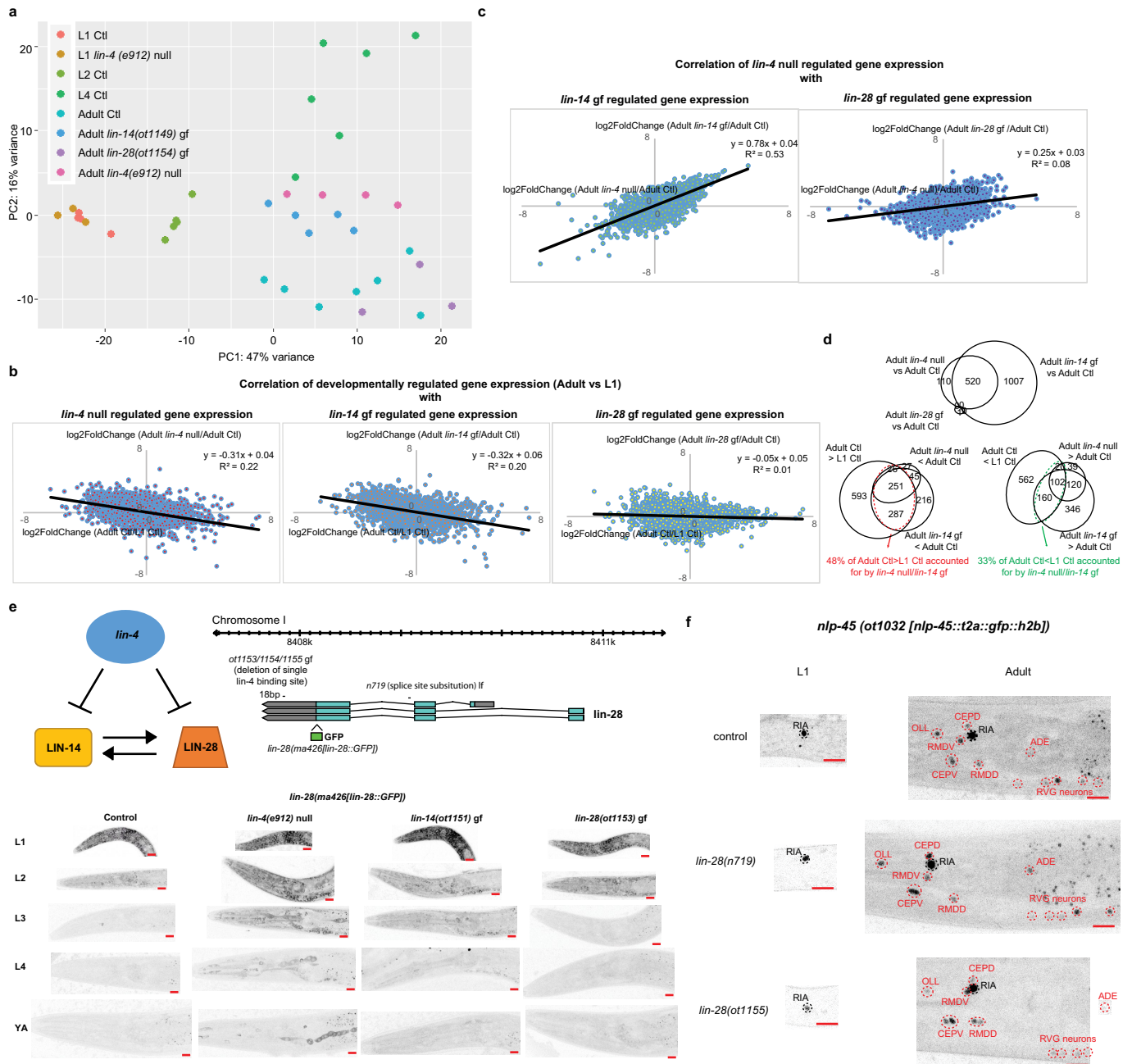
**Extended Data Fig. 4 | Temporal transitions in nervous system gene expression across *C. elegans* post-embryonic development for the receptor-type guanylyl cyclases (rGCs) family.** **a**, Heat map of all neuronally enriched receptor-type guanylyl cyclases (rGCs) across post-embryonic development. Values were z-score normalized and plotted using pheatmap in R studio. Each row represents a single gene, and each column represents a single RNA-seq replicate. For **b–d**, validations of developmentally regulated genes with expression reporters are shown. On top are the scattered dot plots (each point represents a single replicate, n in bracket) of the normalized read counts across all developmental stages from the neuronal INTACT/RNA-seq profiling. Mean  $\pm$  SEM are shown for each stage. Adjusted *P* values ( $P_{adj}$ ), as calculated by DESeq2, for each developmental comparison are below. Below the RNA-seq read count plots are the schematics and allele names of the expression reporters. Below that are representative confocal microscopy images of the expression reporters across development. Specific regions/neurons labelled

with dotted lines: those labelled with black dotted lines/names are not altered developmentally while those labelled with green and red lines/names demonstrate, respectively, decreases and increases in expression across development. Red scale bars (10 $\mu$ m) are on the bottom right of all representative images. For all panels, L1 through L4 represent the first through the fourth larval stage animals. Additional details are included in Supplementary Table 6. **b**, rGC *gcy-5*, as validated with a transcriptional fosmid reporter (*sl2::lxnls::gfp*), shows decreased expression in ASER and increased expression in RIG, as measured with fluorescence intensity, across development. Quantifications of fluorescence intensity are shown at the bottom. Two-sided t-test with post hoc correction *P* values and n in brackets are shown. **c**, rGC *gcy-21*, as validated with a promoter fusion reporter (*gfp*), loses expression in three neuronal classes across the L1->L2 transition. **d**, rGC *gcy-12*, as validated with a promoter fusion reporter (*gfp*), gains expression in A and B type motor neurons across mid/late larval development.



**Extended Data Fig. 5 | Expression of *lin-14* is downregulated in the nervous system amongst other tissues across post-embryonic development in a *lin-4* dependent manner in hermaphrodite animals. a**, Expression of *lin-4* is turned on in the nervous system amongst other tissues during the L1->L2 transition. Schematic of the *lin-4* fosmid expression reagent, in which the *lin-4* pre-miRNA sequence was replaced with YFP, is shown on the left. Representative images of *lin-4* expression in L1 and L2 animals are shown on the right. Ellipse and polygon outline the anterior and lateral/ventral neuronal ganglia respectively. **b**, Expression of *lin-14* is downregulated in the nervous system amongst other tissues across post-embryonic development in a *lin-4* dependent manner in hermaphrodite animals. Schematic of the *lin-14* translational GFP allele, as engineered by CRISPR-Cas9, as well as *lin-14* gain-of-function (gf) alleles (*ot1087/ot1149/ot1150/ot1151*), where a 466bp region containing all seven *lin-4* repressive binding sites is deleted, are shown

on the upper left. All 4 gf alleles represent the same molecular lesion but resulted from independent CRISPR-Cas9 mediated deletions. Quantification of LIN-14::GFP expression in the lateral/ventral ganglion is shown on the upper right. Two-sided t-test with post hoc correction *P* values and *n* (in bracket) are shown. On the bottom are the representative images of the *lin-14*::GFP allele across post-embryonic development in control, *lin-4(e912)*-null, and *lin-14(ot1087) gf* animals. Ellipse and polygon outline the anterior and lateral/ventral neuronal ganglia respectively. Red scale bars (10µm) are on the bottom right of all representative images. Expression of *lin-14* is still detectable in the adult hermaphrodite. *lin-14* expression is upregulated in *lin-4(e912)* null and *lin-14(ot1087) gf* animals across development. The incomplete juvenization of *lin-14* expression across development in the *lin-4* null mutant suggests additional mechanisms beyond *lin-4* that downregulate *lin-14* across post-embryonic development.

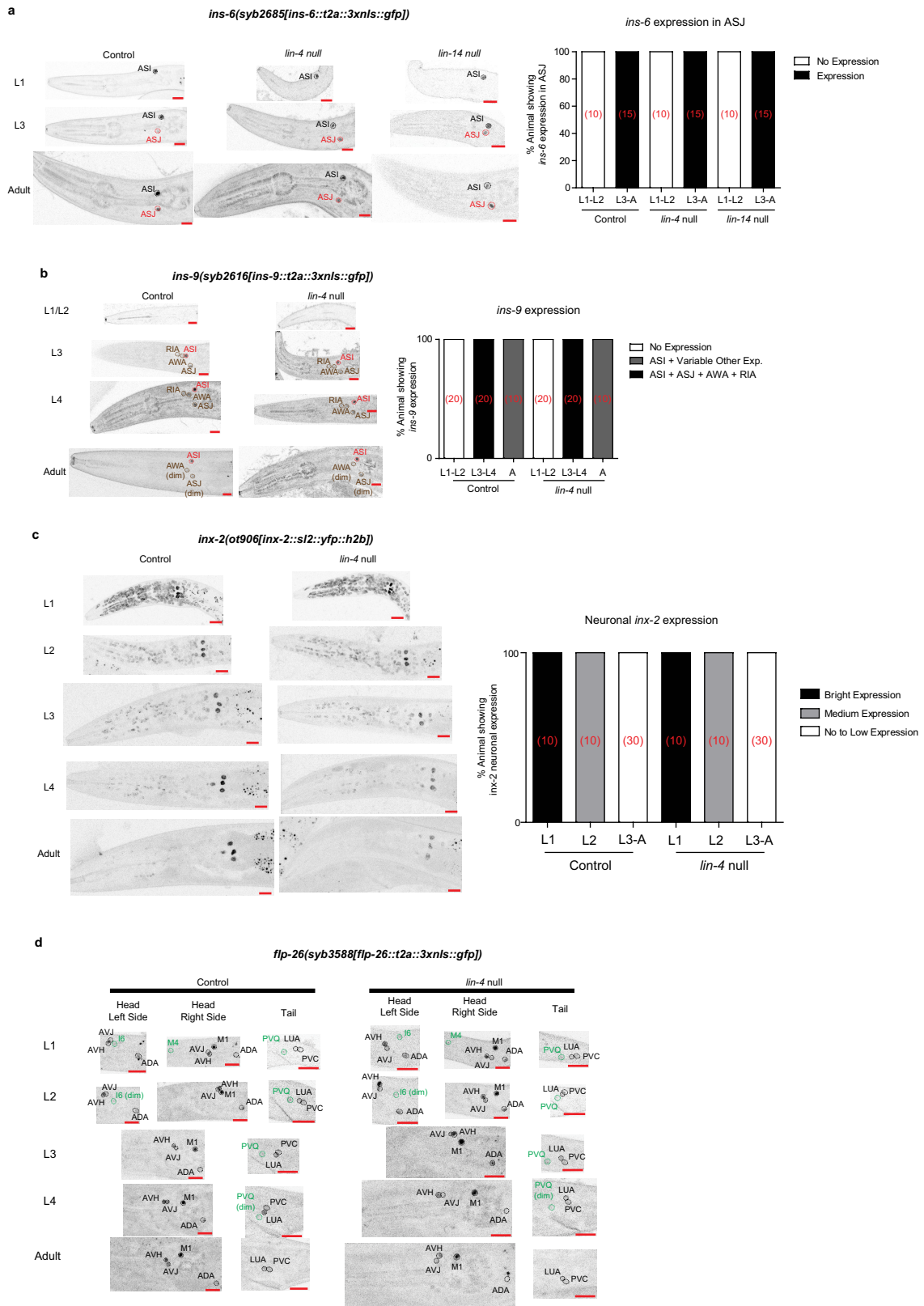


Extended Data Fig. 6 | See next page for caption.

**Extended Data Fig. 6 | *lin-4* controls a subset of the developmentally regulated gene battery through direct repression of *lin-14*, and not *lin-28*.**

**a**, *lin-4(e912)* null mutation juvenizes a subset of the adult control(Ctl) neuronal transcriptome to resemble that of the L1 Ctl neuronal transcriptome through direct de-repression of *lin-14* and not *lin-28*. Principal component analysis (PCA) of the neuronal transcriptomes across post-embryonic development and across genotypes was conducted using DESeq2 in R studio. Each dot represents a replicate in the RNA-seq analysis. **b**, Correlation between developmentally gene expression changes ( $\log_2$ FoldChange[Adult Expression/L1 Expression]) with gene expression changes in *lin-4(e912)* null mutation ( $\log_2$ FoldChange[Adult *lin-4(e912)* null expression/Adult control expression], left), in *lin-14(ot1149)* gain-of-function (gf) mutation ( $\log_2$ FoldChange[Adult *lin-14(ot1149)* gf expression/Adult control expression], middle), and in *lin-28(ot1154)* gf mutation ( $\log_2$ FoldChange[Adult *lin-28(ot1154)* gf expression/Adult control expression], right). Linear regression was fitted through each set of data points, and the equation and  $R^2$  values are shown for each. *lin-4* null and *lin-14* gf mutations accounted for some of the developmentally gene expression changes between L1 and adult, while *lin-28* gf mutation did not. **c**, Correlation between gene expression changes in *lin-4(e912)* null mutation ( $\log_2$ FoldChange[Adult *lin-4(e912)* null expression/Adult control expression]) with gene expression changes in *lin-14(ot1149)* gf mutation ( $\log_2$ FoldChange[Adult *lin-14(ot1149)* gf expression/Adult control expression], left), and in *lin-28(ot1154)* gf mutation ( $\log_2$ FoldChange[Adult *lin-28(ot1154)* gf expression/Adult control expression], right). Linear regression was fitted through each set of data points, and the equation and  $R^2$  values are shown for each. *lin-14* gain of function mutation accounted for most of the changes observed in the *lin-4* null mutation, but *lin-28* gain of function mutation did not. **d**, Top Venn diagram showing that the difference between the adult *lin-4* null neuronal transcriptome compared to the adult control(Ctl) neuronal

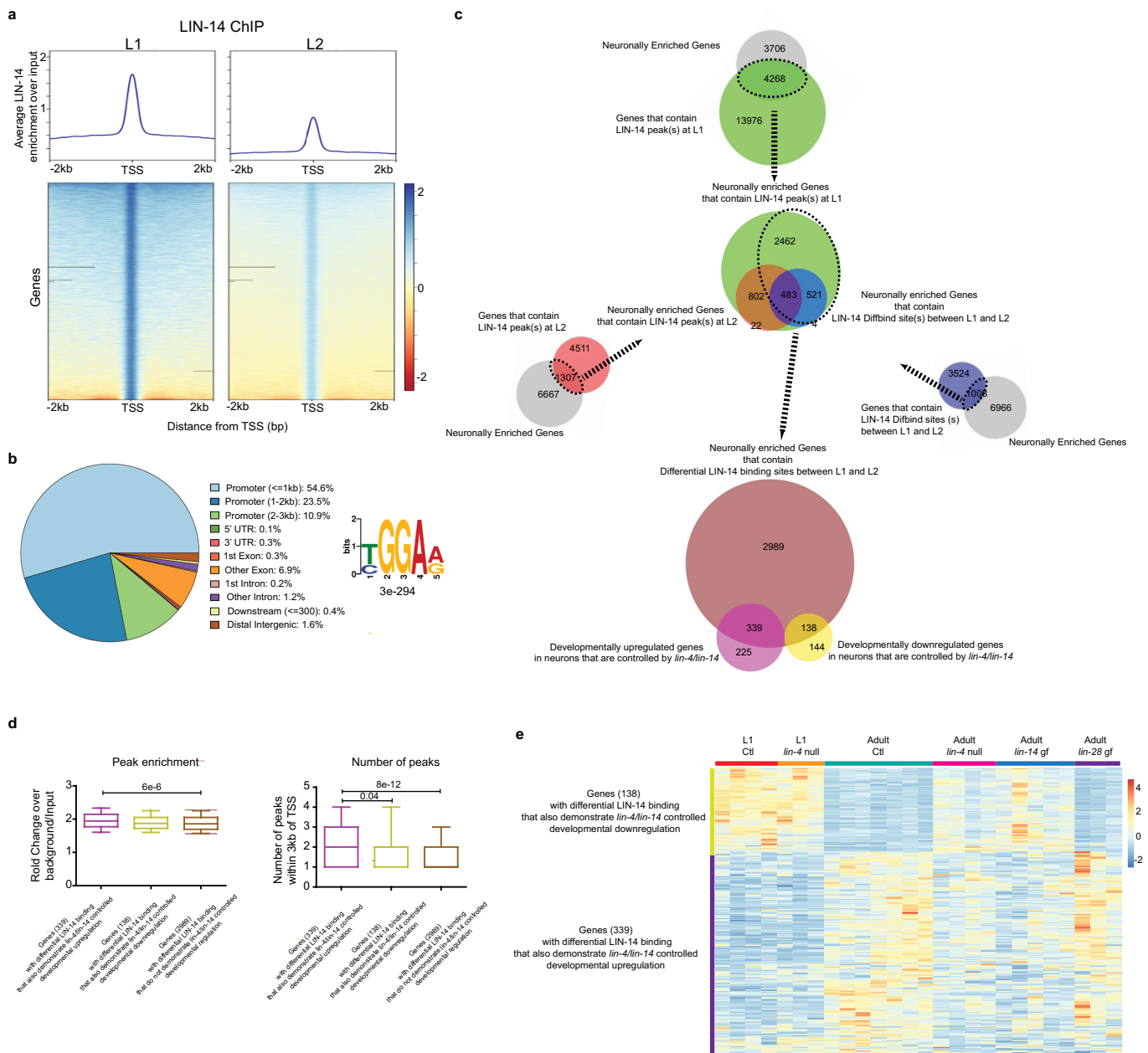
transcriptome is largely recapitulated in the transcriptome of adult *lin-14(ot1149)* gf mutants. Only one gene is significantly different in the adult *lin-28(ot1154)* gf vs adult control comparison and does not overlap with the genes regulated by *lin-4/lin-14*. Bottom left Venn diagram showing that 48% of genes that demonstrate developmental upregulation (adult control(Ctl)>L1 Ctl) are juvenized in the adult *lin-4* null and/or *lin-14(ot1149)* gf animals. Bottom right Venn diagram showing that 33% of genes that demonstrate developmental downregulation (adult control(Ctl)<L1 Ctl) are juvenized in the adult *lin-4* null and/or *lin-14(ot1149)* gf animals. **e**, *lin-4* regulates *lin-28* mainly through *lin-14* and not through direct repression of *lin-28*. On the top left is the schematic of the regulation between *lin-4*, *lin-14* and *lin-28* based upon previous studies. On the top right is the schematic of the *lin-28* translational GFP allele, as engineered by CRISPR-Cas9, as well as *lin-28(ot1153/54/55)* gf and *lin-28(n719)* loss-of-function (lf) alleles. These three gf alleles represent the same molecular lesion (deletion of single *lin-4* binding site in the *lin-28* 3'UTR) but independent CRISPR-Cas9 mediated deletion events. On the bottom are the representative images of the *lin-28* translational GFP allele across post-embryonic development in control, *lin-4(e912)* null, *lin-14(ot1151)* gf, and *lin-28(ot1153)* gf animals. The signal is diffuse and cytoplasmic but can be observed in all tissues including the nervous system in early larval animals. Red scale bars (10 $\mu$ m) are on the bottom right of all representative images. LIN-28 is downregulated across post-embryonic development. *lin-4(e912)* null and *lin-14(ot1151)* gf mutations delay the downregulation of LIN-28, particularly during the L2->L3 transition, while the *lin-28(ot1153)* gf mutation does not. **f**, *lin-28* does not regulate developmental expression pattern of *nlp-45*. Representative images of the *nlp-45* expression reporter in control, *lin-28(n719)* lf and *lin-28(1155)* gf animals. Neurons that are labelled in black are not developmentally regulated while those that are labelled in red are developmentally upregulated. Red scale bars (10 $\mu$ m) are on the bottom right of all representative images.



Extended Data Fig. 7 | See next page for caption.

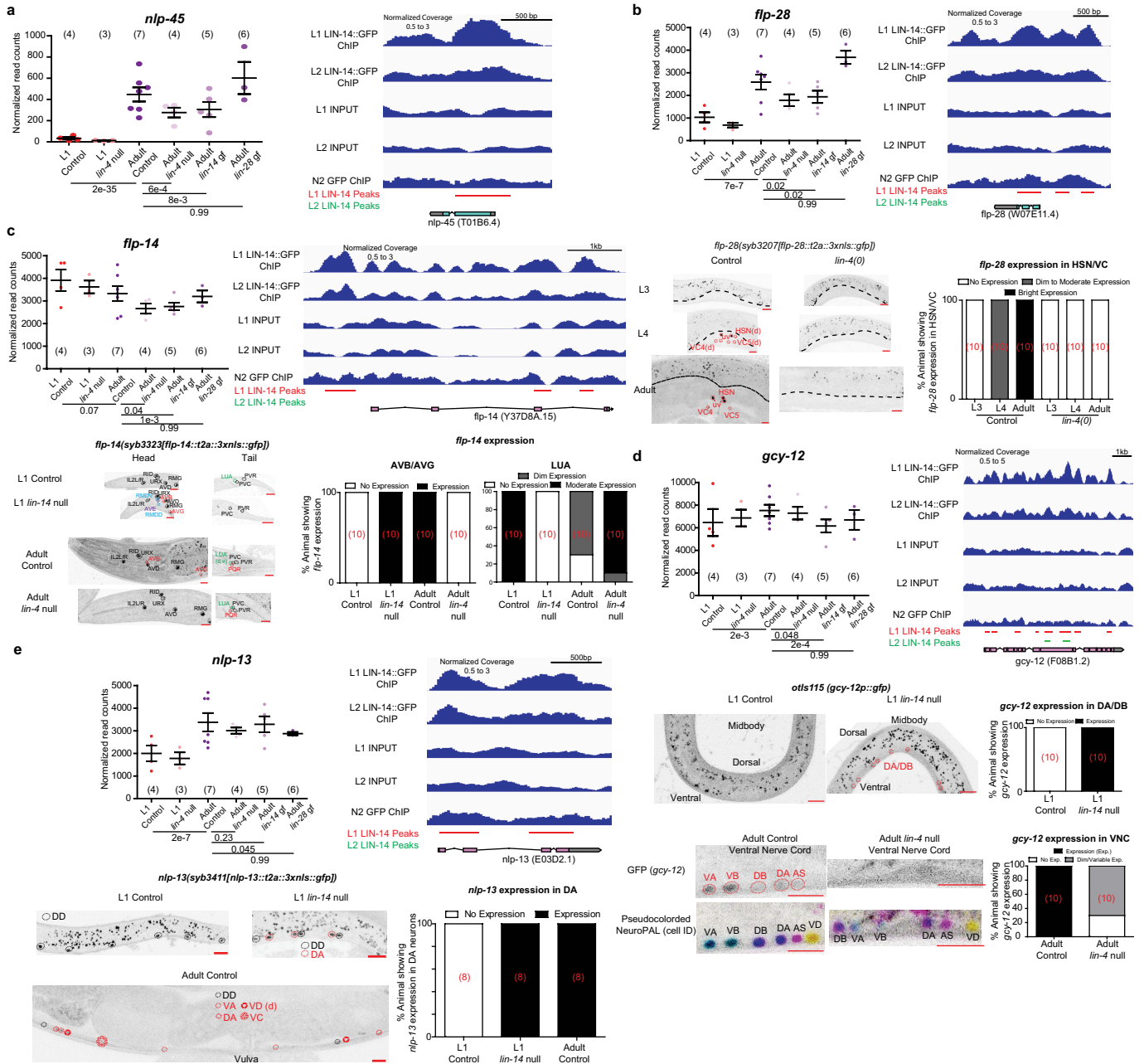
**Extended Data Fig. 7 | Developmentally regulated genes not controlled by *lin-4/lin-14*.** **a**, *ins-6* developmental expression is not regulated by *lin-4* nor *lin-14*. Representative images of the *ins-6* expression reporter in control, *lin-4* null and *lin-14* null animals are shown on the left while quantification of the *ins-6* expression in ASJ is shown on the right (number of animals for each condition is shown in red brackets). **b**, *ins-9* developmental expression is not regulated by *lin-4*. Representative images of the *ins-9* expression reporter in control and *lin-4* null animals are shown on the left while quantification of the *ins-9* expression is shown on the right (number of animals for each condition is shown in red

brackets). **c**, *inx-2* developmental expression is not regulated by *lin-4*. Representative images of the *inx-2* expression reporter in control and *lin-4* null animals are shown on the left while quantification of neuronal *inx-2* expression is shown on the right (number of animals for each condition is shown in red brackets). **d**, *flp-26* developmental expression is not regulated by *lin-4*. Representative images of the *flp-26* expression reporter in control and *lin-4* null animals are shown. Control images for A-D are taken from Extended Data Fig. 3. Red scale bars (10 $\mu$ m) are on the bottom right of all representative images.



**Extended Data Fig. 8 | Decreased LIN-14 binding across L1->L2 transition controls *lin-4/lin-14* dependent transcriptomic changes.** **a**, Decreased LIN-14 binding at promoters of target genes during the L1->L2 transition. Normalized datasets at each developmental stage against respective inputs are generated using the bamCompare function of deepTools2<sup>55</sup>. LIN-14 enrichment around TSS +/- 2kb is then computed using the computeMatrix function and plotted using the plotHeatmap function of deepTools2<sup>55</sup>. **b**, LIN-14 ChIP-seq peak distribution and motif across L1 and L2 animals. The ChIP-seq peak distribution on the left is plotted using CHIPseeker<sup>48</sup>. The consensus binding motif on the right is obtained using MEME-CHIP<sup>49</sup>. **c**, Amalgamation of different methods of assessing differential LIN-14 binding across the L1->L2 transition. Outer three Venn Diagrams on the top are the 32990 LIN-14 peaks in L1 animals within 3kb of the TSS of 18245 genes (green, Supplementary Table 8), the 7240 LIN-14 peaks in L2 animals within 3kb of the TSS of 5818 genes (red, Supplementary Table 9), and the 5267 differential L1 vs L2 LIN-14 binding within 3kb of the TSS of 4532 genes (blue, as determined by DiffBind, Supplementary Table 10), each overlapped with the 7974 neuronally enriched genes. These neuronally enriched peaks in L1 (green), peaks in L2 (red) and differential L1 vs

L2 binding (blue) were overlapped in the middle Venn Diagram to result in the 3466 genes (Supplementary Table 11) that show differential (mostly decreased) L1 vs L2 binding. These 3466 genes overlapped with 339 (60%) of the *lin-4/lin-14* controlled developmentally upregulated genes and 138 (49%) of the *lin-4/lin-14* controlled developmentally downregulated genes. **d**, The 339 genes that showed developmental upregulation (LIN-14 as a repressor) had increased LIN-14 peak enrichment and number of LIN-14 peaks within 3kb of TSS as compared to the 138 genes that showed developmental downregulation (LIN-14 as an activator) or the 2989 genes that show no developmental regulation. Box Whisker plots (10-90 percentile) are used, and two-sided t-test with post hoc correction P values are shown for the comparisons. **e**, Heat map of the developmental up-/down-regulated genes that also had differential LIN-14 binding from **c** across development (L1 and adult) and genotype (Control[Ctl] and *lin-4/lin-14* mutants). Values were z-score normalized and plotted using pheatmap in R studio. Each row represents a single gene, and each column represents a single RNA-seq replicate. The rows are clustered according to gene expression patterns.



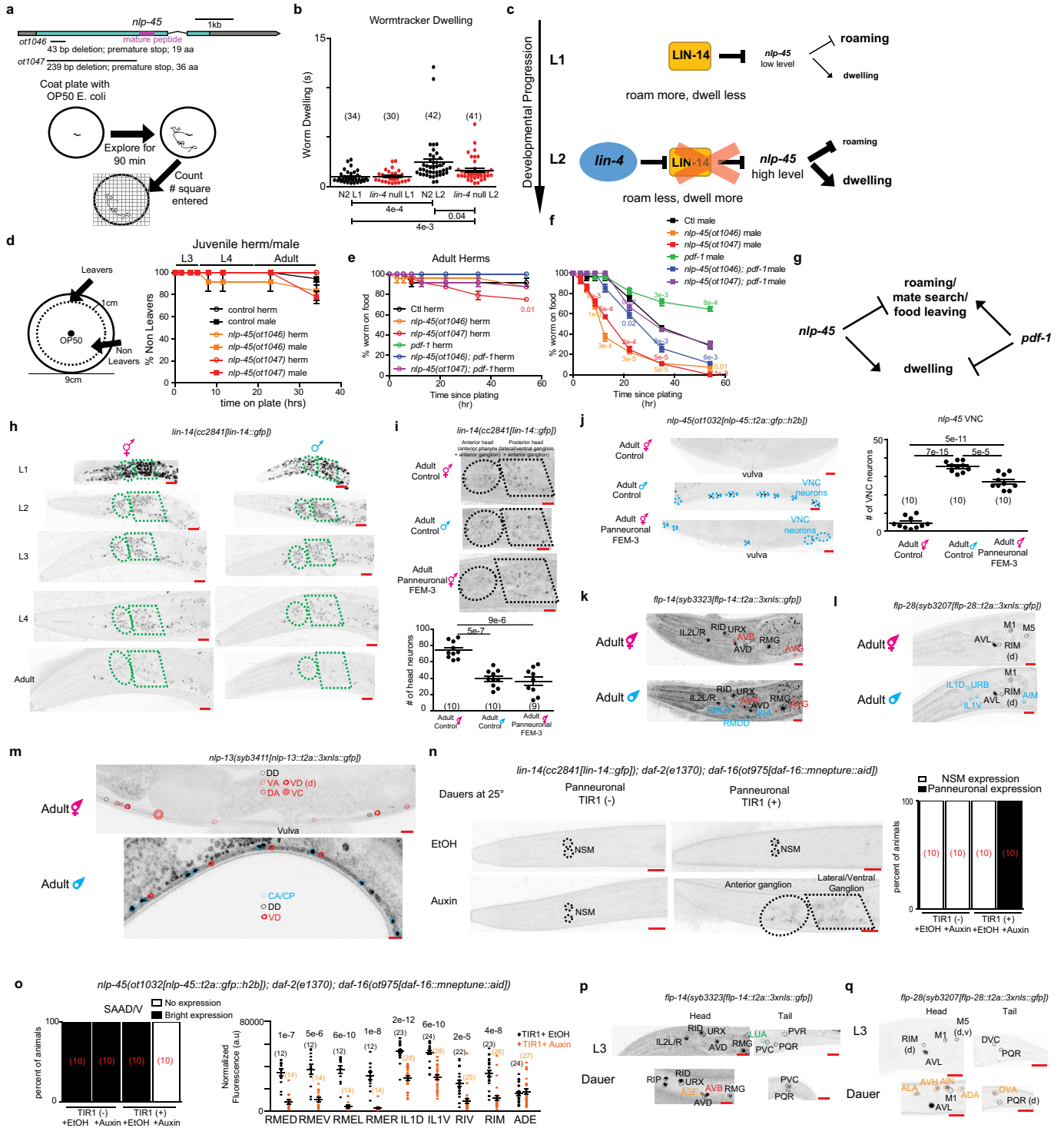
Extended Data Fig. 9 | See next page for caption.

# Article

## Extended Data Fig. 9 | *lin-4/lin-14* control developmental regulation of neuropeptide-encoding and receptor-type guanylyl cyclase (rGC) genes.

For all panels, the plots with normalized RNA-seq read counts for the L1/adult control/heterochronic mutant animals are plotted, with each point representing a replicate (n in bracket) and the mean  $\pm$  SEM shown for each stage, on the upper left. Adjusted  $P$  values ( $P_{adj}$ ), as calculated by DESeq2, for each comparison are below. *lin-4* null/*lin-14* gain-of-function mutations juvenize the expression of all four genes. LIN-14 ChIP-seq binding at each gene is shown on the upper right. All samples from their respective experimental conditions are merged for their respective tracks in IGV. Decrease in LIN-14 binding during the L1->L2 transition is observed for all 4 genes. Representative confocal images under control and mutant conditions are shown in the bottom left. d in brackets denote dim expression, while v in brackets denote variable expression. Red scale bars (10  $\mu$ m) are on the bottom right of all representative images. Quantification of the images are shown on the bottom right (number of animals for each condition is shown in red brackets). **a.** Juvenization of *nlp-45* expression by *lin-4/lin-14* across development as predicted from the neuronal INTACT/RNA-seq profiling and LIN-14 ChIP-seq binding at the *nlp-45* gene. Representative images are shown in Fig. 3a. **b.** *flp-28* expression is gained in hermaphrodite specific neurons (HSN, VC) during transition into late larval/adult stages while the same developmental upregulation is not observed in *lin-4* null mutants. *flp-28* expression in head/tail neurons is not regulated in *lin-4*

null animals (images not shown). Control images are taken from Extended Data Fig. 3f. **c.** *flp-14* loses and gains expression in one (LUA, outlined in green) and two (AVB and AVG, outlined in red) classes of neurons as it enters late larval/adult stages, respectively. *flp-14* expression is de-repressed in the AVB and AVG neurons in L1 *lin-14* null animals while *flp-14* expression is repressed in the LUA neurons in L1 *lin-14* null animals. Consistently, *flp-14* expression in the AVB and AVG neurons are repressed in adult *lin-4* null animals while *flp-14* expression is increased in the LUA neuron as compared to adult control animals. *flp-14* expression is also weakly de-repressed in two classes of neurons that express *flp-14* in the adult male (RMDD/V, outlined in blue) and one additional class of neuron (AVE, outlined in purple) in L1 *lin-14* null animals. Control images are taken from Extended Data Fig. 3i. **d.** *gcy-12* gains expression in the A and B type motor neurons across mid/late larval development. *gcy-12* expression in the A and B type motor neurons is de-repressed in *lin-4* null L1 animals while *gcy-12* expression in the A and B type motor neurons is repressed in the *lin-4* null adult animals as compared to respective control animals. *gcy-12* expression in head/tail neurons is not regulated in *lin-4* null animals (images not shown). **e.** *nlp-13* gains expression in the ventral nerve cord neurons (DA, VA, VD, VC) across development. *nlp-13* expression in the DA neurons is de-repressed in *lin-4* null L1 animals as compared to L1 control animals. Control L1 and adult images are taken from Extended Data Fig. 3j.



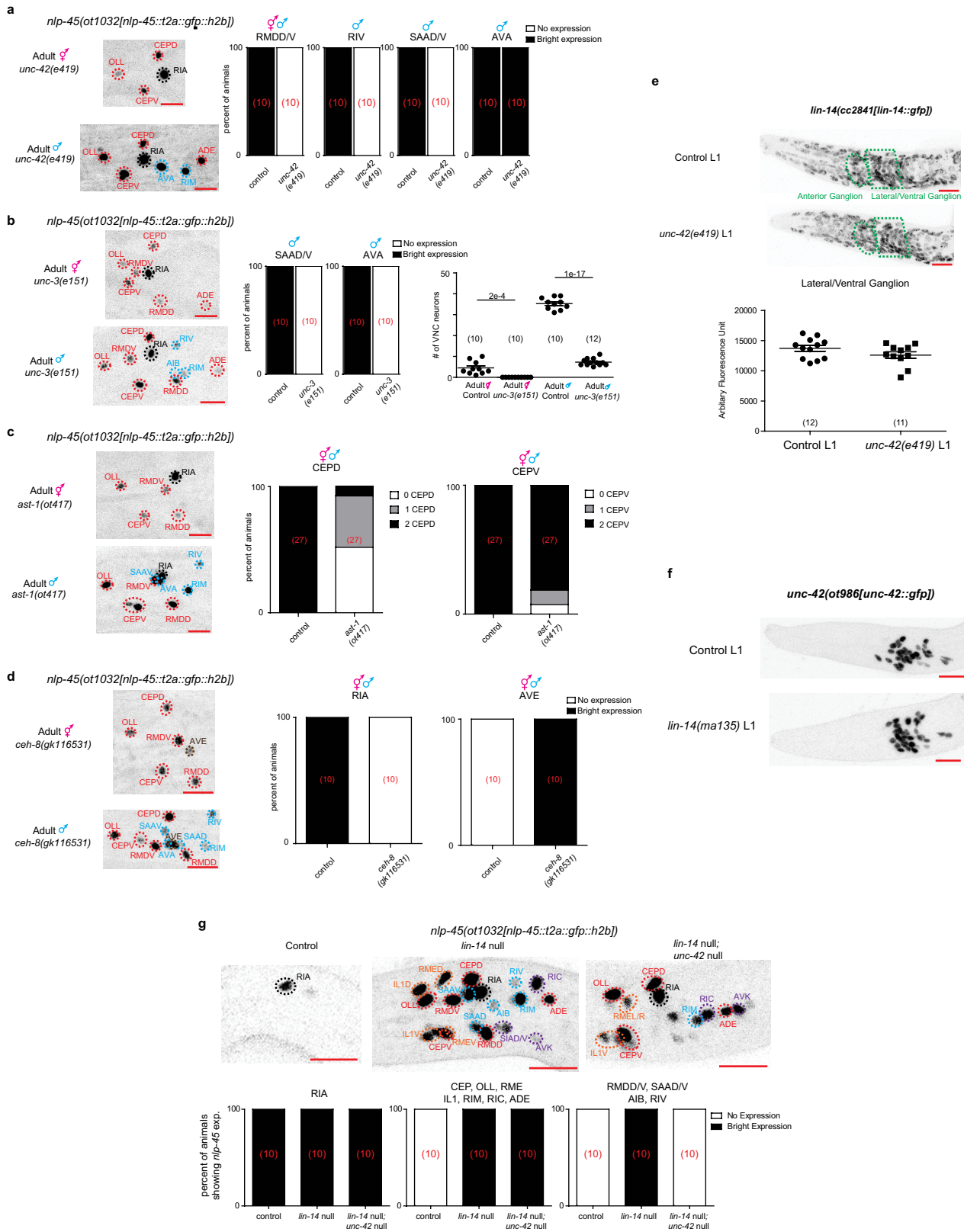
Extended Data Fig. 10 | See next page for caption.

# Article

## Extended Data Fig. 10 | Regulation and function of *nlp-45* across temporal, sexual, and environmental dimensions of post-embryonic development.

**a**, Schematic of *nlp-45* deletion mutants and exploratory assay. **b**, Increased dwelling during L1->L2 transition is partially juvenized in *lin-4(e912)* animals. Mean +/- SEM and n (in bracket) are shown for each condition, and each point of the scatter dot plot represents a single animal. Wilcoxon rank-sum tests and false-discovery rate *q* values for each comparison shown below. **c**, Schematic showing *lin-4/lin-14* regulation of *nlp-45* to alter exploratory behaviour during the L1>L2 transition. **d**, *nlp-45* deletion mutants do not significantly affect the food leaving behaviours of juvenile males/hermaphrodites. Values were plotted as mean +/- SEM of three independent experiments (n=6 animals per independent experiments). **e**, Leaving assay for adult hermaphrodite in *nlp-45* and *pdf-1* mutant animals. Values were plotted as mean +/- SEM of three independent experiments (n=8 animals per independent experiments). Statistical analysis (two-sided t-test with post hoc correction) is only shown for the comparison to respective controls (colour coded respectively). **f**, Leaving assay for adult male in *nlp-45* and *pdf-1* mutant animals. Values plotted as mean +/- SEM of three independent experiments (n=8 animals per independent experiments). Statistical analysis (two-sided t-test with post hoc correction) is only shown for the comparison to respective controls (colour coded respectively). **g**, Schematic of the opposing role of *nlp-45* and *pdf-1* on male food leaving behaviour. **h**, Developmental expression of *lin-14* in hermaphrodites and males. Representative images for the *lin-14(cc2841[lin-14::gfp])* reporter are shown across all developmental stages for both sexes. LIN-14 expression was similarly downregulated in both sexes at early larval stages, its expression in the late larval and particularly in the adult stage was significantly more reduced in the male nervous system compared to that of the hermaphrodite. Ellipse and polygon outline anterior and lateral/ventral neuronal ganglia. Representative images for hermaphrodite are re-used here from Extended Data Fig. 5b for direct side by side comparison with male animals across development. **i**, Pan-neuronal depletion of sex determination master regulator TRA-1, through overexpression of FEM-3, decreases nervous system LIN-14 expression in adult hermaphrodites to mimic that of adult males. Representative microscope images, shown above, are overexposed in comparison to previous *lin-14* reporter images to better show the dim expression in adult males and FEM-3 overexpressed hermaphrodites. The quantifications of head neuron numbers across the three conditions are shown below. The mean +/- SEM and n (in bracket) shown for each condition, and each point of the scatter dot plot represents a single animal. Two-sided t-test with post hoc correction *P* values are shown for each comparison. **j**, Pan-neuronal depletion of TRA-1, through overexpression of FEM-3, masculinizes *nlp-45* expression in adult hermaphrodite VNC. Representative images are shown on the left. Quantifications of VNC neuron numbers are shown on the right. The mean +/- SEM and n (in bracket) are shown for each condition, and each point of the scatter dot plot represents a single animal. Two-sided t-test with post hoc

correction *P* values are shown for each comparison. **k**, Sexually dimorphic expression of *flp-14* in adult hermaphrodites and males. In addition to stronger *flp-14* expression in the AVB neuron (red) as compared to adult hermaphrodites, adult males gain *flp-14* expression in the RMDD/V and SIA neurons (blue). Adult hermaphrodite images are re-used from Extended Data Fig. 3i. **l**, Sexually dimorphic expression of *flp-28* in adult hermaphrodites and males. As compared to adult hermaphrodites, adult males gain *flp-28* expression in the IL1D/V, URB, and AIM neurons (blue). Adult hermaphrodite images are re-used from Extended Data Fig. 3f. **m**, Sexually dimorphic expression of *nlp-13* in adult hermaphrodites and males. In addition to stronger *nlp-13* expression in the VD neurons (red) as compared to adult hermaphrodites, adult males gain *nlp-13* expression in the male specific CA/CP motor neurons (blue) and lose *nlp-13* expression in the DA, VA and hermaphrodite specific VC motor neurons. Adult hermaphrodite images are re-used from Extended Data Fig. 3j. **n**, Pan-neuronal degradation of DAF-16 in auxin-treated dauers leads to pan-neuronal de-repression of *lin-14* in dauer animals. Representative images are on the left while binary quantifications of pan-neuronal expression are shown on the right (number of animals for each condition is shown in red brackets). Animals were grown (from embryo onward) on NGM plates supplemented with OP50 and 4mM auxin in EtOH (indole-3 acetic acid, IAA, Alfa Aesar) at 25 °C to degrade DAF-16 pan-neuronally and to induce dauer formation. As controls, plates were supplemented with the solvent EtOH instead of auxin. Additional control animals without pan-neuronal TIR-1 expression grown on EtOH and auxin were also included for comparison. **o**, Pan-neuronal degradation of DAF-16 in auxin-treated dauers leads to a loss or reduced *nlp-45* expression in several neuronal classes. Representative images are shown in Fig. 4f. Binary quantifications are shown for the SAAD/V neurons (number of animals for each condition is shown in red brackets) while fluorescence quantifications are shown for the RMED/V, RMEL/R, IL1D/V, RIV, RIM, and ADE neurons. The mean +/- SEM and n (in bracket) are shown for each condition, and each point of the scatter dot plot represents a single animal. Two-sided t-test with post hoc correction *P* values are shown for each comparison. **p**, Expression of *flp-14* in dauer animals as compared to L3 animals. Upon entry into dauer, similar to expression pattern in the adult hermaphrodite/male, animals gain *flp-14* expression in the AVB neurons (red) and lose *flp-14* expression in the LUA neurons (green). Additional dauer specific *flp-14* expression is gained in the ASE neurons (orange). Expression in the PVR neurons is also lost in dauer animals. L3 hermaphrodite images are re-used from Extended Data Fig. 3i. **q**, Expression of *flp-28* in dauer animals as compared to L3 animals. Upon entry into dauer, animals gain *flp-28* expression in the ALA, AVH, AIN, ADA, and DVA neurons (labelled in orange) and lose *flp-28* expression in the DVC neurons. L3 hermaphrodite images are re-used from Extended Data Fig. 3f. **d** and **v** in brackets denote dim and variable expression, respectively. Scale bars = 10µm.



Extended Data Fig 11 | See next page for caption.

# Article

## Extended Data Fig 11 | Terminal selector provides spatial specificity to

***nlp-45* expression pattern.** **a**, Regulation of *nlp-45* by cell specific regulator, *unc-42*. Representative images of adult *unc-42(e419)* hermaphrodite and male animals are shown on the left while binary quantifications of *nlp-45* expression in the RMDD/V, RIV, SAAD/V and AVA neurons are shown on the right (number of animals for each condition is shown in red brackets). *nlp-45* expression was lost in all *unc-42* expressing neurons with the exception of AVA in *unc-42* mutant animals. **b**, Regulation of *nlp-45* by cell specific regulator, *unc-3*. Representative images of adult *unc-3(e151)* hermaphrodite and male animals are shown on the left while binary quantifications of *nlp-45* expression in the SAAD/V and AVA neurons are shown in the middle (number of animals for each condition is shown in red brackets). The quantification of ventral nerve cord (VNC) motor neurons is shown on the right. n (in bracket) and two-sided t-test with post hoc correction *P* values are shown. Each point of the scatter dot plot represents a single animal. *nlp-45* expression was lost in *unc-3* expressing head neurons (i.e. SAAD/V, AVA) while severely affected in the VNC in *unc-3* mutant animals. **c**, Regulation of *nlp-45* by cell specific regulator, *ast-1*. Representative images of adult *ast-1(ot417)* hypomorph hermaphrodite and male animals are shown on the left while quantifications of *nlp-45* expression in the CEPD and CEPV neurons are shown on the right (number of animals for each condition is shown in red brackets). *nlp-45* expression was severely affected in the CEPD neurons and slightly affected in the CEPV neurons in the *ast-1* mutant animals.

**d**, Regulation of *nlp-45* by cell specific regulator, *ceh-8*. Representative images of adult *ceh-8(gk116531)* hermaphrodite and male animals are shown on the left while binary quantifications of *nlp-45* expression in the RIA and AVE neurons are shown on the right (number of animals for each condition is shown in red brackets). *nlp-45* expression is lost in the RIA neurons and ectopically gained in the AVE neurons in *ceh-8* mutant animals. **e**, Terminal selector (*unc-42*) does not regulate heterochronic pathway (*lin-14*). On the left are representative images of L1 *lin-14* translational GFP allele worms in control and *unc-42(e419)* backgrounds. On the right is the quantification of fluorescence intensity in the lateral/ventral ganglion of control vs *unc-42(e419)* L1 animals. The mean +/- SEM and n (in bracket) are shown for each condition, and each point of the scatter dot plot represents a single animal. **f**, Heterochronic pathway (*lin-14*) does not regulate terminal selector (*unc-42*). Representative images of L1 *unc-42* translational GFP allele worms in control and *lin-14(ma135)* null backgrounds are shown. **g**, On top are representative images of the *nlp-45* expression reporter in control, *lin-14(0)*, and *lin-14(0);unc-42(0)* L1 animals. On the bottom is are the binary quantifications of *nlp-45* expression in different neuronal subtypes in control, *lin-14(0)*, and *lin-14(0);unc-42(0)* L1 animals (number of animals for each condition is shown in red brackets). *nlp-45* showed precocious expression in *lin-14,unc-42* double mutants, similar to the *lin-14* null mutant alone, except in the neurons (i.e. RMDD/V, SAAD/V) where *unc-42* acts as a terminal selector.

## Reporting Summary

Nature Research wishes to improve the reproducibility of the work that we publish. This form provides structure for consistency and transparency in reporting. For further information on Nature Research policies, see our [Editorial Policies](#) and the [Editorial Policy Checklist](#).

### Statistics

For all statistical analyses, confirm that the following items are present in the figure legend, table legend, main text, or Methods section.

- |     |           |
|-----|-----------|
| n/a | Confirmed |
|-----|-----------|
- The exact sample size ( $n$ ) for each experimental group/condition, given as a discrete number and unit of measurement
  - A statement on whether measurements were taken from distinct samples or whether the same sample was measured repeatedly
  - The statistical test(s) used AND whether they are one- or two-sided  
*Only common tests should be described solely by name; describe more complex techniques in the Methods section.*
  - A description of all covariates tested
  - A description of any assumptions or corrections, such as tests of normality and adjustment for multiple comparisons
  - A full description of the statistical parameters including central tendency (e.g. means) or other basic estimates (e.g. regression coefficient) AND variation (e.g. standard deviation) or associated estimates of uncertainty (e.g. confidence intervals)
  - For null hypothesis testing, the test statistic (e.g.  $F$ ,  $t$ ,  $r$ ) with confidence intervals, effect sizes, degrees of freedom and  $P$  value noted  
*Give  $P$  values as exact values whenever suitable.*
  - For Bayesian analysis, information on the choice of priors and Markov chain Monte Carlo settings
  - For hierarchical and complex designs, identification of the appropriate level for tests and full reporting of outcomes
  - Estimates of effect sizes (e.g. Cohen's  $d$ , Pearson's  $r$ ), indicating how they were calculated

*Our web collection on [statistics for biologists](#) contains articles on many of the points above.*

### Software and code

Policy information about [availability of computer code](#)

Data collection All microscopy images were acquired using the Zen software (Carl Zeiss).

Data analysis Statistical analysis of the automated worm tracking videos was performed as previously described. Briefly, statistical significance between each group was blindly calculated using Wilcoxon rank-sum test and correcting for false-discovery rate. Statistical analysis of RNA-seq comparison was performed using DESeq2 as previously described. Statistical analysis for various aspects of ChIP-seq was done using MACS2, MEME-ChIP and Diffbind. All microscopy fluorescence quantifications were done in the Zen software (Carl Zeiss). All statistical tests for fluorescence quantifications and behavior assays were conducted using Prism (Graphpad) and Excel as described in figure legends.

For manuscripts utilizing custom algorithms or software that are central to the research but not yet described in published literature, software must be made available to editors and reviewers. We strongly encourage code deposition in a community repository (e.g. GitHub). See the Nature Research [guidelines for submitting code & software](#) for further information.

### Data

Policy information about [availability of data](#)

All manuscripts must include a [data availability statement](#). This statement should provide the following information, where applicable:

- Accession codes, unique identifiers, or web links for publicly available datasets
- A list of figures that have associated raw data
- A description of any restrictions on data availability

Raw and processed RNA-seq data is available at GEO accession #GSE158274. Raw and processed ChIP-seq data is available at GEO accession #GSE181288.

## Field-specific reporting

Please select the one below that is the best fit for your research. If you are not sure, read the appropriate sections before making your selection.

Life sciences       Behavioural & social sciences       Ecological, evolutionary & environmental sciences

For a reference copy of the document with all sections, see [nature.com/documents/nr-reporting-summary-flat.pdf](https://www.nature.com/documents/nr-reporting-summary-flat.pdf)

## Life sciences study design

All studies must disclose on these points even when the disclosure is negative.

Sample size	No sample size calculation was performed. Standard number of replicates/animals from previous experience were used.
Data exclusions	For all experiment, a single outlier per experimental group was removed only if it is statistically significant in the Grubb's test ( $p < 0.05$ ).
Replication	All experiments were done with multiple biological replicates and all effects were shown with all replicates. All experiments were repeated at least once independently. At each repeat, all control and experimental conditions were included, and the results of all independent experiments were combined. Whenever representative microscopy images were shown without any quantification, the exact same results were observed in at least 10 animals unless variability is stated.
Randomization	Whenever possible, all samples/animals were randomized.
Blinding	Whenever possible for behavioral analysis, the scoring was done blindly. For all other molecular and microscopy experiments, experimenters were not blind during data collection/analysis.

## Reporting for specific materials, systems and methods

We require information from authors about some types of materials, experimental systems and methods used in many studies. Here, indicate whether each material, system or method listed is relevant to your study. If you are not sure if a list item applies to your research, read the appropriate section before selecting a response.

### Materials & experimental systems

n/a	Involvement in the study
<input type="checkbox"/>	<input checked="" type="checkbox"/> Antibodies
<input checked="" type="checkbox"/>	<input type="checkbox"/> Eukaryotic cell lines
<input checked="" type="checkbox"/>	<input type="checkbox"/> Palaeontology and archaeology
<input type="checkbox"/>	<input checked="" type="checkbox"/> Animals and other organisms
<input checked="" type="checkbox"/>	<input type="checkbox"/> Human research participants
<input checked="" type="checkbox"/>	<input type="checkbox"/> Clinical data
<input checked="" type="checkbox"/>	<input type="checkbox"/> Dual use research of concern

### Methods

n/a	Involvement in the study
<input type="checkbox"/>	<input checked="" type="checkbox"/> ChIP-seq
<input checked="" type="checkbox"/>	<input type="checkbox"/> Flow cytometry
<input checked="" type="checkbox"/>	<input type="checkbox"/> MRI-based neuroimaging

## Antibodies

Antibodies used	Sigma-Aldrich Mouse monoclonal anti-FLAG M2 Cat# F1804 for INTACT nuclei isolation (3ul/reaction); Chromotek GFP-Trap Magnetic Beads (Cat# gtd) for ChIP-seq (25ul/reaction).
Validation	Validation is confirmed as the pulldown of FLAG-tagged nuclei has fluorescent protein at the nuclear membrane that can be visualized as well as by functional validation of the NGS data. LIN-14 ChIP by Chromotek beads were validated with functional changes in gene expression.

## Animals and other organisms

Policy information about [studies involving animals](#); [ARRIVE guidelines](#) recommended for reporting animal research

Laboratory animals	C. elegans. Whenever synchronization of developmental stages was necessary, animals were egg prepped according to standard protocol and synchronized at the L1 stage. They were then plated on food and collected after 8 +/- 1 hrs, 21 +/- 1 hrs, 30 +/- 2hr, 40 +/- 2hrs, and 53 +/- 2hrs for L1, L2, L3, L4, and adult stages, respectively for either molecular or behavioral analysis. These time points were chosen such that the animals were in the middle of each larval stage or relatively early in adulthood for the analysis. Dauer animals were obtained using standard crowding, starvation and high temperature conditions.
Wild animals	No wild animals used.
Field-collected samples	No field-collected samples were used.

## Ethics oversight

No ethics approval was necessary.

Note that full information on the approval of the study protocol must also be provided in the manuscript.

## ChIP-seq

### Data deposition

- Confirm that both raw and final processed data have been deposited in a public database such as [GEO](#).
- Confirm that you have deposited or provided access to graph files (e.g. BED files) for the called peaks.

## Data access links

*May remain private before publication.*

Raw and processed ChIP-seq data is available at GEO accession #GSE181288.

## Files in database submission

Raw fastq sequencing files, bed/tabular files for peak calling/differential binding, and all annotated files for peak and differential binding sites

Genome browser session  
(e.g. [UCSC](#))

not applicable

### Methodology

## Replicates

5 replicates for each developmental stage (L1 and L2) and type (IP and Input)

## Sequencing depth

The libraries were sequenced on Illumina NextSeq 500 machines with 75bp single-end reads.

## Antibodies

Chromotek GFP-Trap Magnetic Beads (Cat# gtd)

## Peak calling parameters

MAC2 default parameters

## Data quality

BAM alignment files were filtered for 20+ MAPQ scores using SAMtools. Correlation among samples was done using DeepTools to ensure separate clustering of ChIP and Input samples. Signal strength of ChIP enrichment using signal extraction scaling (SES) was done using DeepTools. Overlap of ChIP-seq was also done with RNA-seq results, and functional validation using a few gene expression reporters were done.

## Software

After initial quality check, the reads were mapped to WS220 using BWA (Li and Durbin, 2009) and filtered using SAMtools (Li et al., 2009). Peaks were called using MACS2 (Feng et al., 2012). The ChIP-seq peak distribution was calculated and plotted using ChIPseeker (Yu et al., 2015). The consensus binding motif was obtained using MEME-ChIP (Machanick and Bailey, 2011). Differential binding analysis between L1 and L2 was done using Diffbind (Ross-Innes et al., 2012). All peaks and differential binding sites were annotated and assigned to the nearest gene using ChIPseeker (Yu et al., 2015).